# Phospholipid-porphyrin conjugates: deciphering the driving forces behind their supramolecular assemblies

Louis-Gabriel Bronstein[a#], Ágota Tóth[b#], Paul Cressey[a], Véronique Rosilio[a], Florent Di Meo[b*] and Ali Makky[a*]

[a] *Université Paris-Saclay, CNRS, Institut Galien Paris-Saclay, 92296, Châtenay-Malabry, France*

[b] *INSERM U1248 Pharmacology & Transplantation, Univ. Limoges, 2 rue du Prof. Descottes, F-87025, Limoges, France*

[#] Equally contributed

[*] Corresponding authors: florent.di-meo@inserm.fr, ali.makky@universite.paris-saclay.fr

**Abstract**

Phospholipid-porphyrin conjugates (Pl-Por) are nowadays considered as a unique class of building blocks that can self-assemble into supramolecular structures that possess multifunctional properties and enhanced optoelectronics characteristics compared to their monomeric counterparts. However, despite their versatile properties, little is known about the assembling mechanism of Pl-Por conjugates and their molecular organization inside these assemblies. To gain a better understanding on their assembling properties, we synthesized two new series of Pl-Por conjugates with different alkyl sn2-chain lengths linked via an amide bond to either pheophorbide-a ($Ph_x$LPC) or pyropheophorbide-a ($Pyr_x$LPC). By combining a variety of experimental techniques with molecular dynamics simulations, we investigated both the assembling and optical properties of the Pl-Por either self-assembled or when incorporated into lipid bilayers. We demonstrated that Pl-Por conjugates can form assemblies that mimic lipid bilayer structures. Moreover, our results highlight that the non-covalent interactions between porphyrin cores play a central role in controlling both the structure of the lipid bilayer membranes and their subsequent optical properties. The fluidity of the phospholipid bilayer in which the Pl-Por conjugates were incorporated, was shown to play an important role in driving their interaction within the lipid matrix. Altogether, this work could be used as guidelines for the design of new Pl-Por conjugates that self-assemble into bilayer-like supramolecular structures with tunable morphology and optical properties.

**Keywords**

Phospholipid-porphyrin conjugates, supramolecular assemblies, molecular dynamics simulation, lipid bilayer, packing parameter.

## INTRODUCTION

Amphiphilic compounds such as surfactants and phospholipids are molecules that possess both hydrophilic and hydrophobic blocks. When dispersed in water at sufficiently high concentrations (i.e., higher than their critical micelle concentration), they tend to self-assemble into a wide variety of supramolecular structures with a broad range of sizes and shapes such as micelles, vesicles, planar bilayers, nanotubes or nanofibers [1-4]. These organized assemblies offer several functional properties with respect to their monomeric counterparts. In this context, amphiphilic compounds have attracted great attention for biomedical, pharmaceutical, and industrial applications. This is particularly true regarding the assembly of amphiphilic porphyrins [5] or porphyrinoids [6-7] into supramolecular structures designed for photoactivatable drug delivery devices [6-11] as well as light-harvesting nanosystems [12-13]. Amphiphilic porphyrin derivatives appear as very promising scaffolds since they can self-assemble into supramolecular structures [5] with adjustable photophysical properties and biomedical outcomes [14]. Among the amphiphilic porphyrins that have been designed so far for the development of photo-activatable drug delivery systems, the phospholipid-porphyrin (Pl-Por) conjugates initially proposed by Gang Zheng's group [9, 15-16] belong to the most versatile compounds for biomedical applications. These conjugates are made of pyropheophorbide-a or bacteriochlorophyll-a photosensitizers linked to the sn2 hydroxyl group of 1-lysophosphatidylcholine (C16) via an esterification reaction. Such Pl-Por conjugates self-assemble into liposome-like nanostructures named "porphysomes" [9] which exhibit a highly organized packing of the porphyrin molecules with improved optical and photophysical properties [9, 14] when compared to unconjugated porphyrin derivatives. In addition, such packed porphyrin organization enables the use of these assemblies in multiple applications including photothermal therapy (PTT), photo-triggered drug release, photoacoustic imaging or fluorescence imaging [9] and photodynamic therapy (PDT) following their disassembly at the

tumor site [9, 17]. The shape and morphology of the self-assembled structures of amphiphiles are usually predicted using simple models of the dimensionless geometric packing parameter ($P = v/a.l$) which is defined as the ratio between the volume of the hydrophobic part ($v$) of the amphiphiles and the optimal cross sectional surface area ($a$) of the hydrophilic headgroup times the length ($l$) of hydrophobic chains in their all-trans conformation [1-2]. Amphiphiles with packing parameters lower than 1/3 or between 1/3 and ½ form spherical and worm-like micelles, respectively. On the other hand, while double-tailed phospholipids exhibiting packing parameters lying between ½ and 1 form bilayers, those with P values larger than 1 self-assemble into inverted hexagonal phases ($H_{II}$) [2, 4].

Despite the versatile feature of Pl-Por conjugates as building blocks for the design of multifunctional nanoplatforms [18-21], the impact of the geometrical packing parameter on the formation and properties of their assemblies, as well as on their mixing with host phospholipids, remains unclear [8, 22-24]. Pl-Por building blocks initially consisting of a bulky porphyrin core directly attached to the hydroxyl group in sn2 position of 1-lysophosphatidylcholine (C16) [9] would exhibit a large area of the polar headgroup with concomitant mismatch between the length of the alkyl chain in sn1 position and the adjacent porphyrin. Thus, along the same line of thought of phospholipids assemblies, Pl-Por conjugates are not expected to form bilayers, unless other driving forces or parameters are involved. This can be likely overcome by adding a linker between phosphatidylcholine headgroup and the porphyrin moiety. Changing the length of the alkyl chain in the sn2 position is expected to reduce the chain length mismatch between the two hydrophobic tails of the conjugate. It was expected that chromophores grafted to a longer chain should align with the sn1 C16 alkyl chain improving the lateral packing properties due to the reduction of the length mismatch between the two chains. Indeed, Carter et al. [22] used molecular dynamics simulations to demonstrate that conjugating devinyl hexyloxyethy-pyropheophorbide

(a pyro-a derivative) which possesses an hexyl ether moiety at its extremity, enabled the formation of stable bilayers with superior packing properties when compared to the pyro-a conjugate. Such high packing properties of HPPH-conjugates were related to the presence of hexyl ether moiety which provided a better space filling between the two bilayer leaflets [22]. Beside the mismatch between the two chains, changing the porphyrin structure should also play an important role in the intermolecular interaction between porphyrin cores which in turn might impact their stability and their photophysical properties.

In the present work, we describe the syntheses of two new series of Pl-Por conjugates exhibiting different alkyl chain lengths in sn2 position and linked via an amide bond to either pheophorbide-a ($Ph_x$LPC) or pyropheophorbide-a ($Pyr_x$LPC) (Scheme 1). The self-assemblies of the synthesized Pl-Por conjugates as well as their incorporation into liposomes were then characterized in terms of morphology, optoelectronic properties and thermodynamics using cryogenic transmission electron microscopy (Cryo-TEM), absorbance/fluorescence spectroscopy and differential scanning calorimetry (DSC). Experimental observations were supported by molecular dynamics simulations providing an atomic-scale and dynamic pictures of porphyrin conjugate self-assemblies. The present joint experimental and computational investigations aim to provide reliable insights for understanding the role of (i) the porphyrin structure, (ii) the length of the linker and (iii) the role of surrounding lipid environment on the properties of Pl-Por assemblies.

## EXPERIMENTAL SECTION

### Chemicals

Pheophorbide-a (Pheo-a, ≥ 95%, mixture of diastereomers, Mw = 592.69 g/mol) and pyropheophorbide-a (Pyro-a, ≥ 95%, Mw = 534.66 g/mol) were purchased from Livchem Logistics GmbH (Frankfurt, Germany). N-α-t-β-butyloxycarbonyl-glycin (≥ 99%, Mw = 175.18 g/mol), N-t-butyloxycarbonyl-β-alanine (≥ 99%, Mw = 189.21 g/mol), N-t-butyloxycarbonyl-γ-aminobutyric acid (≥ 99%, Mw = 203.24 g/mol) and HCl:dioxane (4M) were purchased from abcr GmbH (Karlsruhe, Germany).

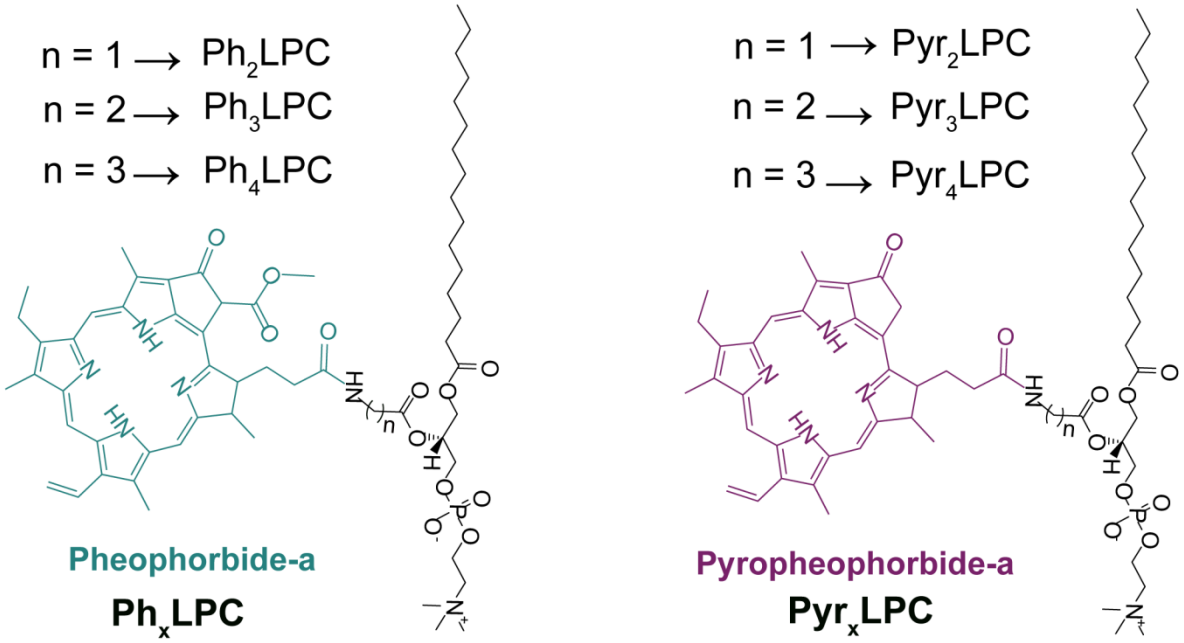


**Scheme 1.** Structure of lipid-porphyrin conjugates $Ph_xLPC$ and $Pyr_xLPC$ bearing pheophorbide-a and pyropheophorbide-a chromophore respectively.

Amberlite® IRA-400 chloride form, N-(3-dimethylaminopropyl)-N′-ethylcarbodiimide hydrochloride (EDC.HCl, ≥ 98%, Mw = 191.70 g/mol), 1-hydroxybenzotriazole hydrate (≥ 98%, Mw =135.12 g/mol), 4-(dimethylamino)pyridine (DMAP, ≥ 99%, Mw = 122.17 g/mol), Dowex® 50WX8-100 ion exchange resin (hydrogen form), N,N-diisopropylethylamine (DIPEA, 99%, Mw = 129.24 g/mol), HEPES (99.5%, Mw = 238.31 g/mol), sodium chloride (NaCl, 99%, Mw = 58.44 g/mol), anhydrous chloroform (≥ 99%, stabilized with amylenes) and triethylamine (Mw = 101.19 g/mol) were purchased from Sigma Aldrich (St. Louis, MO, USA). The phospholipid 1-

palmitoyl-2-hydroxy-sn-glycero-3-phosphocholine (16:0 Lyso-PC, 99%, 495.63 g/mol) was purchased from Avanti Polar Lipids (Alabaster, AL). The ultrapure water ($\gamma$ = 72.2 mN/m at 22° C) (MQ water) used in all experiments was produced by a Millipore Milli-Q® Direct 8 water purification System, with a resistivity of 18.2 MΩ.cm. Silica (60M, 0.04-0.063 mm) used for column chromatography was purchased from Macherey-Nagel GmbH (Düren, Germany). Solvents were purchased from CARLO ERBA Reagents (Val de Reuil, France). All compound and solvents were used without further purification.

**Synthesis of the modified phospholipids and the lipid-porphyrin conjugates**

**BocNH-Gly-LPC (2-(((tert-butoxycarbonyl)glycyl)oxy)-3-(palmitoyloxy)propyl (2-(trimethylammonio)ethyl) phosphate)**

16:0 Lyso-PC (100 mg, 0.2 mmol) and N-alpha-t-butyloxycarbonyl-glycin (105 mg, 0.6 mmol) were mixed in 5 ml of anhydrous chloroform and stirred until clear mixture was obtained. DMAP (76 mg, 0.9 mmol) and EDC.HCl (116 mg, 0.6 mmol) were added separately, in anhydrous chloroform (3 mL). Glass beads (5 g, 2 mm) previously washed with ethanol, and dried under vacuum were added to the mixture. The mixture was then sonicated for 12 h with the temperature kept under 25 °C throughout the reaction. Additional N-alpha-t-butyloxycarbonyl-glycin (50 mg, 0.15 mmol), DMAP (20 mg, 0.24 mmol) and EDC.HCl (20 mg, 0.10 mmol) were added after 4 hours of sonication to ensure complete conversion. Once 16:0 Lyso-PC was fully converted, the mixture was incubated with DOWEX (Dowex® 50WX8 hydrogen form) for 30 minutes to remove DMAP, filtered, and concentrated *in vacuo* to yield a colorless oil. The crude mixture was suspended in 4 mL MQ water and purified with 1000 Da MWCO dialysis membrane over 24 h, after dialysis the water was removed by lyophilization to yield BocNH-Gly-LPC as a white powder which was stored at -20 °C (119 mg, yield 91 %). BocNH-Gly-LPC rf = 0.42-0.45,

chloroform-methanol-water (65:25:4)). $^{1}$H NMR (details in Figure S1) (300 MHz, $CDCl_3$) δ (ppm) = 5.89 (bs, 1H, NH), 5.25 (m, 1H, $C_{20}$), 4.28-4.17 (m, 4H, $C_{40}$ & $C_{19}$), 4.07-3.83 (m, 2H, $C_{21}$), 3.74 (s, 2H, $C_{39}$), 3.36 (s, 9H, $C_{42-44}$), 3.05 (bs, 2H, $C_{30}$), 2.28 (t, 2H,J=7.5Hz, $C_{15}$), 1.55 (qu, 2H J=6.0 Hz, $C_{14}$), 1.42 (s, 9H, $C_{36-38}$), 1.25 (s, 24H, $C_{2-13}$), 0.87 (3H, t, J=6.9 Hz, $C_1$).; $^{13}$C NMR (75 MHz, $CDCl_3$) δ = 174.17 (C=O), 173.32 (C=O), 156.74 (C=O), 79.61, 71.62 (CH), 67.09, 63.33, 59.92, 55.06 ($N(CH_3)_3$), 34.68, 32.50, 32.10, 30.28, 30.11, 29.93, 29.90, 29.76, 29.06 ($C(CH_3)_3$), 25.87, 25.46, 23.26, 14.67 ($CH_3$). MS (ESI) for $[C_{31}H_{61}N_2O_{10}P]^+$; calculated: 652.3 $[M+H]^+$; observed: 653.4 $[M+Na]^+$; observed: 675.4

**BocNH-Ala-LPC (2-((3-((tert-butoxycarbonyl)amino)propanoyl)oxy)-3-(palmitoyloxy)propyl (2-(trimethylammonio)ethyl) phosphate)**

16:0 Lyso-PC (100 mg, 0.2 mmol) and N-t-butyloxycarbonyl-beta-alanine (114 mg, 0.6 mmol) were mixed in 5 ml of anhydrous chloroform and stirred until clear mixture was obtained. DMAP (76 mg, 0.9 mmol) and EDC (116 mg, 0.6 mmol) were added separately, in anhydrous chloroform (3 mL). Glass beads (5 g, 2 mm) previously washed with ethanol, and dried under vacuum were added to the mixture. The mixture was then sonicated for 12 h with the temperature kept under 25 °C throughout the reaction. Additional N-t-butyloxycarbonyl-beta-alanine (50 mg, 0.3 mmol), DMAP (20 mg, 0.24 mmol) and EDC.HCl (20 mg, 0.10 mmol) were added after 4 hours of sonication to ensure complete conversion. Once 16:0 Lyso-PC was fully converted, the mixture was incubated with DOWEX (Dowex® 50WX8 hydrogen form) for 30 minutes to remove DMAP, filtered, and concentrated in vacuo to yield a colorless oil. The crude mixture was suspended in 4 mL MQ water and purified with 1000 Da MWCO dialysis membrane over 24 h, after dialysis the water was removed by lyophilization to yield BocNH-Ala-LPC as a white powder which was stored at -20 °C. Pure compound (125 mg, white powder, yield 87%).

BocNH-Ala-LPC rf = 0.45-0.47, chloroform-methanol-water (65:25:4)). $^{1}$H NMR (details in Figure S2) (300 MHz, $CDCl_3$) δ (ppm) = 5.51 (bs, 1H, NH), 5.21 (m, 1H, $C_{20}$), 4.32-4.16 (m, 4H, $C_{40}$-$C_{19}$), 4.06-3.94 (s, 2H, $C_{21}$), 3.81 (s, 2H, $C_{39}$), 3.36 (s, 9H, $C_{42\text{-}44}$), 2.86 (bs, 2H, $C_{45}$), 2.55 (t, 2H, J=6Hz,$C_{30}$), 2.28 (t, 2H, J=7.5Hz, $C_{15}$), 1.58 (qu, 2H,J= 6Hz, $C_{14}$), 1.42 (s, 9H, $C_{36\text{-}38}$), 1.25 (s, 24H, $C_{2}$-$_{13}$), 0.87 (3H, t, $C_1$). $^{13}$C NMR (75 MHz, $CDCl_3$) δ = 173.77 (C=O), 172.98 (C=O), 156.33 (C=O), 79.15, 71.14 (CH), 66.47, 62.91, 59.46, 54.52 ($N(CH_3)_3$), 34.24, 32.07, 31.66, 29.86, 29.71, 29.50, 29.35, 28.63 ($C(CH_3)_3$), 25.43, 25.03, 22.83, 14.25 ($CH_3$). MS (ESI) for $[C_{45}H_{72}N_2O_{10}P]^+$; calculated: 666.3 observed: 667.43 observed: $[M+Na]^+$; 689.41.

**BocNH-γBuA-LPC (2-((4-((tert-butoxycarbonyl)amino)butanoyl)oxy)-3-(palmitoyloxy)propyl (2-(trimethylammonio)ethyl) phosphate)**

16:0 Lyso-PC (100 mg, 0.2 mmol) and N-t-butyloxycarbonyl-γ-aminobutyric acid (122mg, 0.6 mmol) were mixed in 5 ml of anhydrous chloroform and stirred until clear mixture was obtained. DMAP (76 mg, 0.6 mmol) and EDC (116 mg, 0.6 mmol) were added separately, in anhydrous chloroform (3 mL). Glass beads (5 g, 2 mm) previously washed with ethanol, and dried under vacuum were added to the mixture. The mixture was then sonicated for 12 h with the temperature kept under 25 °C throughout the reaction. Additional N-t-butyloxycarbonyl-γ-aminobutyric acid (50 mg, 0.1 mmol), DMAP (20 mg, 0.24 mmol) and EDC.HCl (20 mg, 0.10 mmol) were added after 4 hours of sonication to ensure complete conversion. Once 16:0 Lyso-PC is full converted, the mixture was incubated with DOWEX (Dowex® 50WX8 hydrogen form) for 30 minutes to remove DMAP, filtered, and concentrated under vacuum to yield a colorless oil. The crude mixture was suspended in 4 mL MQ water and purified with 1000 Da MWCO dialysis membrane during 24 h, after dialysis the water was removed by lyophilization to yield BocNH-γBuA-LPC as a white powder which was stored at -20 °C (102 mg, white powder, yield 74%). BocNH-

γBuA-LPC rf = 0.46-0.48, chloroform-methanol-water (65:25:4)). $^{1}$H NMR (details in Figure S3) (300 MHz, $CDCl_3$) δ (ppm) = 5.36 (bs, 1H, NH), 5.19 (m, 1H, $C_{20}$), 4.37-4.15 (m, 4H, $C_{40}$-$C_{19}$), 3.94 (m, 2H, $C_{21}$), 3.71 (m, 2H, $C_{19}$) 3.69 (MeOH), 3.28 (s, 9H, $C_{42-44}$), 3.10 (m, 2H, $C_{46}$), 2.37 (m, 2H, $C_{30}$), 2.28 (m, 2H, J=7.8Hz, $C_{15}$), 1.80 (qu, 2H, J=7.1Hz, $C_{45}$), 1.56 (m, 2H, $C_{14}$), 1.42 (s, 9H, $C_{38-36}$), 1.25 (s, 24H, $C_{2-13}$), 0.87 (t, 3H, $C_1$). $^{13}$C NMR (75 MHz, $CDCl_3$) δ = 173.77 (C=O), 172.98 (C=O), 156.33 (C=O), 79.15, 71.14 (CH), 66.47, 63.79, 62.91, 59.46, 58.78, 54.52 ($N(CH_3)_3$), 34.24, 32.07, 31.66, 29.86, 29.50, 29.35, 28.63 ($C(CH_3)_3$), 25.43, 25.03, 22.83, 14.25 ($CH_3$). MS (ESI) for $[C_{33}H_{65}N_2O_{10}P]^+$; calculated: 680.3 $[M+H]^+$; observed: 681.5; $[M+Na]^+$; observed: 703.5.

**$Ph_2$LPC**

BocNH-Gly-LPC (25 mg, 0.04 mmol) was suspended in 1-4, dioxane and few drops of HCl:dioxane (4M) were added. The mixture was stirred at room temperature until a white precipitate formed. The mixture was dried *in vacuo*, after which it was dissolved in methanol (5 mL) and incubated with Amberlite IRA-400 chloride form (25 mg) for 30 minutes. The resin was removed by filtration and washed with methanol before being dried under vacuum to yield the deprotected $H_2N$-Gly-LPC, which was used without further purification. The deprotected lipid $H_2N$-Gly-LPC (20 mg, 0.04 mmol) was dissolved in anhydrous chloroform (3 mL). EDC (23 mg, 0.12 mmol), 1-hydroxybenzotriazole hydrate (16 mg, 0.12 mmol) and Pheo-a (25 mg, 0.042 mmol) were added to the mixture. After that triethylamine (50 µL) was added and the mixture stirred at room temperature for 24h in the dark under $Ar_{(g)}$. The chloroform and triethylamine were removed *in vacuo*. The crude was resuspended in minimum amount of chloroform and purified by gradient silica gel column chromatography (chloroform-methanol 80:20 (v:v) to chloroform-methanol-water 65:25:4 (v:v); rf = 0.39). The pure product was dried *in vacuo*,

resuspended in water (2 mL) and then lyophilized to yield the product as a fluffy black powder which was stored at -20°C (21.6 mg, black powder, 48% yield). $^{1}$H NMR (details in Figure S4) (400 MHz, DMSO-$d_6$) δ (ppm) = 9.63 (s, 1H, $C_{38}$), 9.27 (s, 1H, $C_{40}$), 8.86 (s, 1H, $C_{51}$), 8.43 (s, 1H, $NH_{37}$), 8.12-8.04 (dd, 1H, J=11.6-17.4 Hz, $C_{68}$), 6.39 (s, 1H, $NH_{47}$), 6.32-6.28 (d, 1H, J= 18Hz, $C_{69}$), 6.16-6.13 (d, 1H, J= 12Hz, $C_{69}$), 5.05 (m, 1H, $C_{20}$), 4.57 (m, 1H, $C_{63}$), 4.22 (m, 1H, $C_{56}$), 4.12 (m, 1H, $C_{55}$), 4.04 (m, 4H, $C_{19}$-$C_{28}$), 3.82 (s, 3H, $C_{70}$), 3.76 (m, 4H, $C_{21}$-$C_{65}$) , 3.60 (s, 3H, $C_{64}$), 3.57 (m, 2H, $C_{27}$), 3.37 (s, 3H, $C_{66}$), 3.12 (s, 9H, $C_{30\text{-}32}$), 3.09 (m, 2H, $C_{36}$), 3.07 (s, 3H, $C_{80}$), 2.37-2.19 (m, 4H, $C_{72}$-$C_{73}$), 2.10 (t, 2H, $C_{15}$), 1.78 (d, 3H, $C_{71}$), 1.56 (t, 3H, J= 7.1 Hz, $C_{67}$), 1.05-0.80 (m, 28H, $C_{2\text{-}14}$, $C_{65}$), 0.76 (t, 3H, J= 7.2 Hz, $C_1$), -1.9 (bs, 1H, $NH_{53}$). $^{13}$C NMR (101 MHz, DMSO) δ = 189.16, 173.10, 172.63, 172.31, 169.46, 169.27, 161.74, 154.61, 150.13, 148.81, 144.76, 141.41, 137.13, 135.89, 135.67, 135.25, 132.02, 128.68, 127.98, 126.96, 124.27, 122.80, 118.95, 109.90, 105.17, 104.42, 96.63, 93.76, 79.29, 71.03, 65.25 ,64.28, 62.85, 62.01, 58.68, 53.12, 52.68, 51.23, 49.39, 45.29, 40.68, 39.52, 33.13, 32.28, 31.13, 30.01, 28.79, 28.67, 28.51, 28.38, 28.21, 24.08, 22.85, 21.95, 18.31, 17.19, 13.80, 11.81, 11.58, 10.49, 8.36. MS (MALDI-TOF) for $[C_{61}H_{87}N_6O_{12}P]^+$; calculated: 1126.63 $[M+H]^+$; observed: 1127.64.

**$Pyr_2$LPC**

BocNH-Gly-LPC (21 mg, 0.031 mmol) was suspended in 1-4, dioxane and few drops of HCl:dioxane (4M) was added. The mixture was stirred at room temperature until a white precipitate formed. The mixture was dried *in vacuo*, after which it was dissolved in methanol (5 mL) and incubated with Amberlite IRA-400 chloride form (25 mg) for 30 minutes. The resin was removed by filtration and washed with methanol before being dried under vacuum to yield the deprotected $H_2$N-Gly-LPC, which was used without further purification. The deprotected lipid $H_2$N-Gly-LPC (18 mg, 0.031 mmol) was dissolved in anhydrous chloroform (3 mL). EDC.HCl

(12.2 mg, 0.09 mmol), 1-hydroxybenzotriazole hydrate (12.2 mg, 0.09 mmol) and pyro-a (20 mg, 0.032 mmol) were added to the mixture. After that triethylamine (50 µL) was added and the mixture stirred at room temperature for 24h in the dark under $Ar_{(g)}$. The chloroform and triethylamine were removed *in vacuo*. The crude was resuspended in minimum amount of chloroform and purified by gradient silica gel column chromatography (chloroform-methanol 80:20 (v:v) to chloroform-methanol-water 65:25:4 (v:v); rf = 0.41). The pure product was dried *in vacuo*, resuspended in water (2 mL) and then lyophilized to yield the product as a fluffy black powder which was stored at -20 °C (16.3 mg, 58 % yield). $^{1}$H NMR (details in Figure S5) (400 MHz, DMSO-$d_6$) δ (ppm) = 9.64 (s, 1H, $C_{38}$), 9.36 (s, 1H, $C_{40}$), 8.85 (s, 1H, $C_{51}$), 8.53 (m,1H, $NH_{37}$), 8.15 (dd, 1H, J=11.6-17.8 Hz, $C_{68}$), 6.34 (dd, 1H, J= 1.5-17.8 Hz, $C_{69}$), 6.17 (dd, 1H, 1.5-11.6 Hz, $C_{69}$), 5.25-5.03 (d ,1H, J=20 Hz, $C_{63}$), 5.11-5.06 (d, 1H, J= 20Hz, $C_{63}$), 5.03 (m, 1H, $C_{20}$), 4.58 (dt, 1H, $C_{56}$), 4.26 (m, 2H, $C_{21}$), 4.10 (dd, 1H, $C_{55}$), 4.04 (m, 2H, $C_{28}$), 3.86 (m, 2H, $C_{19}$), 3.77 (m, 2H, $C_{73}$), 3.66 (q, 2H, $C_{65}$), 3.57 (s, 3H, $C_{70}$), 3.51 (m, 2H, $C_{27}$), 3.41 (s, 3H, $C_{64}$), 3.16 (s, 3H, $C_{66}$), 3.12 (s, 11H, $C_{31-33}$, $C_{36}$), 2.67 (m, 1H, $C_{72}$), 2.29 (m, 1H, $C_{72}$), 2.07 (t, 2H, $C_{15}$), 1.79 (d, 3H, $C_{71}$), 1.60 (t, 3H, $C_{67}$), 1.07-0.65 (m, 29H, $C_{1-14}$). $^{13}$C NMR (101 MHz, DMSO) δ = 200.80 (C=O), 178.88 (C=O), 173.65 (C=O), 172.00, 169.98, 164.46, 149.77, 148.71, 140.77, 136.79, 135.75, 135.48, 132.85, 129.55, 126.84, 121.55, 119.16, 114.78, 110.71, 103.69, 98.23, 96.40, 94.24, 65.91, 63.02, 62.69, 59.00, 58.87, 55.73, 53.59, 49.86, 47.99, 45.76, 33.58, 31.60, 31.56, 29.45, 29.24, 29.14, 29.10, 28.98, 28.82, 28.64, 24.54, 23.36, 22.42, 19.05, 17.85, 14.29. MS (MALDI-TOF) for $[C_{59}H_{85}N_6O_{10}P]^+$; calculated: 1068.62 $[M+H]^+$; observed: 1069.64.

**$Ph_3$LPC**

BocNH-Ala-LPC (25 mg, 0.04 mmol) was suspended in 1-4, dioxane and few drops of HCl:dioxane (4M) were added. The mixture was stirred at room temperature until a white precipitate formed. The mixture was dried *in vacuo*, after which it was dissolved in methanol (5 mL) and incubated with Amberlite IRA-400 chloride form (25 mg) for 30 minutes. The resin was removed by filtration and washed with methanol before being dried under vacuum to yield the deprotected $H_2N$-Ala-LPC, which was used without further purification. The deprotected lipid $H_2N$-Ala-LPC (23 mg, 0.04 mmol) was dissolved in anhydrous chloroform (3 mL). EDC (25 mg, 0.12 mmol), 1-hydroxybenzotriazole hydrate (16 mg, 0.12 mmol) and pheo-a (24 mg, 0.042 mmol) were added to the mixture. After that triethylamine (50 µL) was added and the mixture was stirred at room temperature for 24h in the dark under $Ar_{(g)}$. The chloroform and triethylamine were removed *in vacuo*. The crude was resuspended in minimum amount of chloroform and purified by gradient silica gel column chromatography (chloroform-methanol 80:20 (v:v) to chloroform-methanol-water 65:25:4 (v:v); rf = 0.36). The pure product was dried *in vacuo*, resuspended in water (2 mL) and then lyophilized to yield the product as a fluffy black powder which was stored at -20°C (19 mg, black powder, 42% yield*).* $^{1}$H NMR (details in Figure S6) (400 MHz, DMSO-$d_6$) δ (ppm) = 9.35 (s, 1H, $C_{38}$), 8.96 (s, 1H, $C_{40}$), 8.81 (s, 1H, $C_{51}$), 8.46 (s, 1H, $NH_{37}$ ), 7.87 (dd, 1H, J = 17.7-11.6 Hz, $C_{68}$), 6.4 (m, 1H, $NH_{47}$), 6.17-6.13 (dd, 1H, J = 1.5-18 Hz, $C_{69}$) , 6.04-6.01 (dd, 1H, J= 1.5-11.6 Hz, $C_{69}$), 5.05 (m, 1H, $C_{20}$), 4.60 (m, 1H, $C_{63}$), 4.22 (m, 2x1H, $C_{55}$-$C_{56}$), 4.06 (m, 4H, $C_{19}$-$C_{28}$), 3.86 (m, 5H, $C_{70}$-$C_{21}$), 3.53 (s, 5H, $C_{64}$ – $C_{65}$), 3.28 (m, 5H, $C_{66}$, $C_{27}$), 3.14 (s, 9H, $C_{30\text{-}32}$), 2.93 (t, 2H, $C_{81}$) 2.82 (s, 3H, $C_{80}$), 2.57 (m, 2H, $C_{72}$) 2.44 (m, 2H, $C_{36}$), 2.18 (m, 2H, $C_{73}$), 2.06 (t, 2H, J= 7.2 Hz, $C_{15}$), 1.80 (d, 3H, J= 7.1 Hz, $C_{71}$), 1.44 (m, 3H, $C_{67}$), 1.11-0.87 (m, 26H, $C_{2\text{-}14}$), 0.72 (t, 3H, J=.7.0 Hz, $C_1$). $^{13}$C NMR (101 MHz, DMSO) δ = 189.11 (C=O), 173.04 (C=O), 172.49 (C=O), 171.82 (C=O), 170.71, 169.22, 161.91, 154.41, 149.97, 148.73, 144.57, 141.28, 137.02, 135.71, 135.52, 135.09, 131.88, 128.60, 128.30, 122.63,

121.03, 105.12, 104.23, 96.47, 93.71, 70.82, 65.37, 64.20, 62.65, 62.14, 58.35, 53.06, 52.58, 51.23, 49.35, 45.20, 39.52, 34.74, 34.07, 33.10, 32.46, 31.09, 30.09, 28.75, 28.59, 28.47, 28.42, 28.15, 27.*34*, 24.12, 22.81, 21.90, 18.20, 17.09, 13.73, 11.71, 11.49, 10.36, 8.52. MS (MALDI-TOF) for $[C_{62}H_{89}N_6O_{12}P]^+$; calculated: 1140.64 $[M+H]^+$; observed: 1141.62.

**$Pyr_3$LPC**

BocNH-Ala-LPC (20 mg, 0.03 mmol was suspended in 1-4, dioxane and few drops of HCl:dioxane (4M) was added. The mixture was stirred at room temperature until a white precipitate formed. The mixture was dried in vacuo, after which it was dissolved in methanol (5 mL) and incubated with Amberlite IRA-400 chloride form (25 mg) for 30 minutes. The resin was removed by filtration and washed with methanol before being dried under vacuum to yield the deprotected $H_2N$-Ala-LPC, which was used without further purification. The deprotected lipid $H_2N$-Ala-LPC (18 mg, 0.03 mmol) was dissolved in anhydrous chloroform (3 mL). EDC (17 mg, 0.09 mmol), 1-hydroxybenzotriazole hydrate (12 mg, 0.09 mmol) and pyro-a (17 mg, 0.032 mmol) were added to the mixture. After that triethylamine (50 µL) was added and the mixture stirred at room temperature for 24h in the dark under $Ar_{(g)}$. The chloroform and triethylamine were removed in vacuo. The crude was resuspended in minimum amount of chloroform and purified by gradient silica gel column chromatography (chloroform-methanol 80:20 (v:v) to chloroform-methanol-water 65:25:4 (v:v); rf = 0.39). The pure product was dried in vacuo, resuspended in water (2 mL) and then lyophilized to yield the product as a fluffy black powder which was stored at -20°C (23.2 mg, black powder, 72% yield). $^1$H NMR (details in Figure S7) (400 MHz, DMSO-$d_6$,) δ (ppm) = 9.53 (s, 1H, $C_{39}$), 9.28 (s, 1H, $C_{41}$), 8.83 (s, 1H, $C_{52}$), 8.56 (m,1H, $NH_{38}$), 8.10 (dd, 1H, J=11.6-17.8 Hz, $C_{69}$), 6.30 (dd, 1H, J= 1.5-17.8 Hz, $C_{70}$), 6.15 (dd,

1H, 1.5-11.6 Hz, C70), 5.21 (d ,1H, J=20 Hz, $C_{64}$), 5.06 (d, 1H, J= 20Hz, $C_{64}$), 5.05 (m, 1H, $C_{20}$), 4.56 (dt, 1H, $C_{57}$), 4.23 (m, 2H, $C_{28}$), 4.11 (dd, 1H, $C_{56}$), 4.03 (m,2H, $C_{19}$), 3.83 (m, 2H, $C_{21}$), 3.59 (q, 2H, $C_{66}$), 3.53 (s, 3H, $C_{71}$), 3.49 (m, 2H, $C_{27}$) 3.38 (s, 3H, $C_{65}$), 3.35 (s, 2H, $C_{74}$), 3.10 (s, 12H, $C_{30-32}$, $C_{67}$), 2.96 (q, 2H, $C_{37}$), 2.62 (m, 1H, $C_{73}$), 2.47 (t, 2H, $C_{36}$), 2.25 (m, 1H, $C_{73}$), 2.06 (m, 2H, $C_{15}$), 1.77 (d, 3H, $C_{72}$), 1.56 (d, 3H, $C_{68}$), 1.22-0.83 (m, 26H, $C_{2-14}$), 0.73 (t, 3H, $C_1$). $^{13}$C NMR (101 MHz, DMSO) δ = 201.04 (C=O), 191.94 (C=O), 178.00 (C=O), 174.38, 154.57, 150.37, 148.45, 145.10, 137.63, 136.33, 135.72, 135.69, 132.11, 129.50, 128.27, 125.62, 124.13, 123.23, 121.59, 121.55, 121.49, 104.52, 96.87, 94.23, 65.96, 65.91, 62.66, 58.85, 58.80, 53.57, 51.86, 49.84, 47.98, 45.89, 40.00, 35.32, 34.71, 33.62, 32.97, 31.60, 29.46, 29.24, 29.09, 28.99, 28.90, 28.64, 24.64, 23.35, 22.42, 19.02, 17.82, 14.28, 12.37, 12.03, 11.24, 9.15. MS (MALDI-TOF) for $[C_{60}H_{87}N_6O_{10}P]^+$; calculated: 1082.62 $[M+H]^+$; observed: 1083.67.

**$Ph_4$LPC**

BocNH-γBuA-LPC (18 mg, 0.03 mmol) was suspended in 1-4, dioxane and few drops of HCl:dioxane (4M) was added. The mixture was stirred at room temperature until a white precipitate formed. The mixture was dried *in vacuo*, after which it was dissolved in methanol (5 mL) and incubated with Amberlite IRA-400 chloride form (25 mg) for 30 minutes. The resin was removed by filtration and washed with methanol before being dried under vacuum to yield the deprotected $H_2$N-γBuA-LPC, which was used without further purification. The deprotected lipid $H_2$N-γBuA-LPC (14 mg, 0.03 mmol) was dissolved in anhydrous chloroform (3 mL). EDC (9 mg, 0.09 mmol), 1-hydroxybenzotriazole hydrate (8 mg, 0.09 mmol) and pheo-a (16 mg, 0.03 mmol) was added to the mixture. After that triethylamine (50 µL) was added and the mixture stirred at room temperature for 24h in the dark under $Ar_{(g)}$. The chloroform and triethylamine were removed *in vacuo*. The crude was resuspended in minimum amount of chloroform and

purified by gradient silica gel column chromatography (chloroform-methanol 80:20 (v:v) to chloroform-methanol-water 65:25:4 (v:v); rf = 0.42). The pure product was dried *in vacuo*, resuspended in water (2 mL) and then lyophilized to yield the product as a fluffy black powder which was stored at -20°C (13.2 mg, 52% yield). $^{1}$H NMR (details in Figure S8) (400 MHz, DMSO-$d_6$) δ (ppm) = 9.23 (s, 1H, $C_{38}$), 8.81 (1H, s, $C_{40}$), 8.76 ( s, 1H, $C_{51}$), 8.10 (s, 1H, $NH_{37}$), 7.84-7.72 (dd, 1H, J= 11.6-17.7 Hz, $C_{68}$), 6.40 (s, 1H, $NH_{47}$), 6.09-6.04 (dd, 1H, J=1.3-18 Hz, $C_{69}$), 5.97-5.94 (dd, 1H, J=1.3-11.5 Hz, $C_{69}$), 5.05 (m, 1H, $C_{20}$), 4.58 (m, 1H, $C_{63}$), 4.22 (m, 2x1H, $C_{55}$-$C_{56}$), 4.05 (m, 4H, $C_{19}$-$C_{28}$), 3.86 (s, 3H, $C_{70}$), 3.77 (m, 2H, $C_{21}$), 3.60 (m, 2H, $C_{65}$), 3.45 (m, 2H, $C_{27}$), 3.50 (s, 3H, $C_{64}$), 3.22 (s, 3H, $C_{66}$), 3.14 (s, 9H, $C_{30\text{-}32}$), 2.70 (s, 3H, $C_{80}$), 2.36-2.18 (m, 6H, $C_{36}$-$C_{82}$-$C_{73}$), 2.10 (2H, t, J=7.1 Hz, $C_{15}$), 1.80 (d, 3H, J= 5.2 Hz, $C_{71}$) , 1.63 (m, 2H, $C_{81}$), 1.38 (t, 3H, J= 7.1 Hz, $C_{67}$), 1.04-0.78 (m, 28H, $C_{2\text{-}14}$), 0.68 (t, 3H, J=7.1 Hz, $C_1$), -2.15 (bs, 1H, $NH_{53}$). $^{13}$C NMR (101 MHz, DMSO) δ = 189.14 (C=O), 172.93 (C=O), 172.55 (C=O), 172.09 (C=O), 171.64, 169.33, 161.80, 154.31, 149.89, 148.75, 144.38, 141.26, 136.99, 135.44, 134.97, 131.78, 128.49, 128.18, 123.56, 122.47, 118.61, 110.27, 105.10, 104.04, 96.33, 93.58, 70.62, 65.41, 64.26, 62.67, 62.28, 58.43, 53.12, 52.61, 51.24, 49.42, 39.52, 37.78, 33.15, 32.57, 31.08, 28.73, 28.57, 28.47, 28.41, 28.18, 24.49, 24.15, 22.81, 21.90, 18.10, 17.02, 13.71, 11.65, 11.46, 10.20. MS (MALDI-TOF) for $[C_{63}H_{91}N_6O_{12}P]^+$; calculated: 1176.64 $[M+H]^+$; observed: 1177.64.

**$Pyr_4$LPC**

BocNH-γBuA-LPC (20 mg, 0.03 mmol) was suspended in 1-4, dioxane and few drops of HCl:dioxane (4M) was added. The mixture was stirred at room temperature until a white precipitate formed. The mixture was dried *in vacuo*, after which it was dissolved in methanol (5 mL) and incubated with Amberlite IRA-400 chloride form (25 mg) for 30 minutes. The resin was removed by filtration and washed with methanol before being dried under vacuum to yield the

deprotected $H_2N$-γBuA-LPC, which was used without further purification. The deprotected lipid $H_2N$-γBuA-LPC (17 mg, 0.03 mmol) was dissolved in anhydrous chloroform (3 mL). EDC (25 mg, 0.12 mmol), 1-hydroxybenzotriazole hydrate (16 mg, 0.12 mmol) and Pyro-a (17 mg, 0.032 mmol) was added to the mixture. After that triethylamine (50 µL) was added and the mixture stirred at room temperature for 24h in the dark under $Ar_{(g)}$. The chloroform and triethylamine were removed *in vacuo*. The crude was resuspended in minimum amount of chloroform and purified by gradient silica gel column chromatography (chloroform-methanol 80:20 (v:v) to chloroform-methanol-water 65:25:4 (v:v); rf = 0.38). The pure product was dried in vacuo, resuspended in water (2 mL) and then lyophilized to yield the product as a fluffy black powder which was stored at -20°C (14 mg, black powder, 44% yield). $^{1}$H NMR (details in Figure S9) (400 MHz, DMSO-$d_6$) δ (ppm) = 9.64 (s, 1H, $C_{40}$), 9.36 (s, 1H, $C_{42}$), 8.85 (s, 1H, $C_{53}$), 8.53 (m,1H, $NH_{39}$), 8.15 (dd, 1H, J=11.6-17.8 Hz, $C_{70}$), 6.34 (dd, 1H, J= 1.5-17.8 Hz, $C_{71}$), 6.17 (dd, 1H, 1.5-11.6 Hz, $C_{71}$), 5.25-5.03 (d ,1H, J=20 Hz, $C_{65}$), 5.11-5.06 (d, 1H, J= 20Hz, $C_{65}$), 5.03 (m, 1H, $C_{20}$), 4.58 (dt, 1H, $C_{56}$), 4.26 (m, 2H, $C_{28}$), 4.10 (dd, 1H, $C_{57}$), 4.04 (m,2H, $C_{19}$), 3.77 (m, 2H, $C_{21}$), 3.66 (q, 2H, $C_{67}$), 3.57 (s, 3H, $C_{72}$), 3.51 (m, 2H, $C_{27}$), 3.41 (s, 3H, $C_{66}$), 3.16 (s, 3H, $C_{68}$), 3.12 (s, 11H, $C_{31\text{-}33}$, $C_{75}$), 2.64 (m, 1H, $C_{74}$), 2.43 (m, 2H, $C_{38}$), 2.30 (m, 2H, $C_{36}$), 2.18 (m, 1H, $C_{74}$), 2.07 (m, 2H, $C_{15}$), 1.79 (d, 3H, $C_{73}$), 1.65 (m, 2H, $C_{37}$), 1.59 (t, 2H, $C_{69}$), 1.25-0.8 (m, 26H, $C_{2\text{-}13}$), 0.75 (t, 3H, $C_1$). $^{13}$C NMR (101 MHz, DMSO) δ = 194.69 (C=O), 172.13 (C=O), 171.75 (C=O), 171.56, 171.48, 161.00, 153.36, 149.28, 143.79, 140.15, 136.50, 135.00, 134.58, 134.22, 130.95, 129.36, 128.43, 126.95, 122.99, 121.87, 118.12, 105.31, 103.15, 95.67, 93.05, 70.25, 70.17, 65.02, 62.25, 61.93, 58.05, 57.20, 52.73, 50.97, 49.01, 47.09, 39.52, 37.43, 32.73, 32.19, 30.79, 30.68, 30.05, 28.51, 28.32, 28.12, 28.06, 27.97, 27.74, 24.22, 23.72, 22.41, 21.50, 17.97,

16.78, 13.33, 11.36, 10.98, 10.10. MS (MALDI-TOF) for $[C_{61}H_{89}N_6O_{10}P]^+$; calculated: 1096.64 $[M+H]^+$; observed: 1097.69.

**Preparation and characterization of self-assembled structures or liposomes**

The self-assembled structures as well as liposomes incorporating lipid-porphyrin conjugates were prepared by the thin lipid film hydration method[24-25] followed by extrusion of the vesicles suspension as described previously [24]. Mixtures of lipids and lipid-porphyrin conjugate were prepared in chloroform: methanol (9:1 v/v). After removing the organic solvent under vacuum at 45°C, the resulting film was rehydrated with 1 mL of HEPES buffer, to get a final and total concentration in lipids of 2 mM. The mixture was vortexed at 70°C for 5 min. The suspension was then extruded 21 times through a 200 nm pore-sized polycarbonate membrane, while maintaining the temperature at 70°C. The hydrodynamic diameter was measured by dynamic light scattering (DLS) (Nano ZS90, Malvern). All measurements were carried out at 25 °C. By comparison with standards at specific concentrations of lipid-porphyrin conjugates in Triton/HEPES solution, their content in the assemblies was evaluated by measuring the absorbance at 667 nm of each sample after assemblies disruption by addition of Triton TX-100 (1% v:v) in the suspension using CARY 300 Bio UV–visible spectrophotometer (Varian, USA).

**Cryogenic transmission electron microscopy (Cryo-TEM)**

The self-assembled structures made of lipid-porphyrin conjugates or their mixtures with phospholipids were deposited on perforated carbon-coated, copper grid (TedPella, Inc) which was immediately plunged into a liquid ethane bath cooled with liquid nitrogen (-180 °C) and then mounted on a cryo holder [26]. Cryo-Transmission electron microscopy (TEM) measurements were then performed using a JEOL 2200FS (JEOL USA, Inc., Peabody, MA, U.S.A.) working under

an acceleration voltage of 200 kV (Institut Curie). Electron micrographs were recorded by a CCD camera (Gatan, Evry, France).

**Absorption and Fluorescence Measurements**

UV–visible absorption measurements were carried out on a CARY 300 Bio UV–visible spectrophotometer (Varian, USA). Fluorescence emission spectra were recorded on a Perkin-Elmer LS-50B luminescence spectrometer (MA, USA) equipped with a red sensitive photomultiplier. Excitation of porphyrins was performed at the maximum of the Soret band (415 nm) at a concentration of ~ 4µM of Pl-Por.

**Differential scanning calorimetry (DSC) experiments**

DSC measurements were carried out using a VP-DSC calorimeter (MicroCal, Inc., Northampton, MA, USA). To ensure that thermal equilibrium was reached, three successive heating/cooling scans were recorded from 10 °C to 60 °C at a scan rate of 60 °C/h. Pure DPPC liposomes or DPPC/lipid-porphyrin conjugates lamellar suspensions were prepared at a final concentration of 2 mM in HEPES buffer (10mM, NaCl 150mM, pH 7.4). All experiments were performed in duplicate.

**Force fields and system builder**

The Amber force field (FF) Lipid17[27-28] was used to described DPPC and POPC lipid molecules. $Ph_x$LPC and $Pyr_x$LPC parameters were derived from GAFF2[29] and Lipid17 FF and are available in supplementary information. Atomic charges of porphyrin core and linker moieties were derived applying the AM1-bcc method using the antechamber package. Lipid bilayer membranes were solvated using the TIP3P water model [30] using a hydration level set up at *ca.* 40 water

molecules per lipid. Given the size of porphyrin core and possible interdigitation of lipid tails in porphyrin rings, lipid bilayer membranes were all built by a homemade script (available upon request) and by taking advantage of the packmol-membrane package. Briefly, 3+3, 13+13 and 64+64 molecules of Pl-Por respectively corresponding to 2.5 mol %, 10 mol % and pure Pl-Por systems were put on two grids for upper and lower leaflets. Initial box and grid sizes were defined to prevent steric clash between porphyrins accounting DPPC and POPC area per lipids [31]. Initial area per lipid used to build pure Pl-Por system was set up to 90 $Å^2$ to avoid steric clashes. Packmol was also used to (i) build DPPC or POPC lipids around $Pyr_x$LPC and $Ph_x$LPC molecules and (ii) solvate with water molecules. Na+ and $Cl^-$ ions were then randomly added in water to match NaCl = 0.154 M. It is worth mentioning that for pure Pl-Por systems, both trans and cis configurations were considered regarding porphyrin A-ring.

**Molecular dynamics simulations**

MD simulations were carried out using the CPU- and GPU-PMEMD (Particle Mesh Ewald Molecular Dynamics) codes available in Amber20[32{D.A. Case, 2021 #1545}]. Systems were first minimized. Then, they were thermalized in *(N,V,T)* ensemble up to 298K for 250ps steps in which lipid PC polar head groups were restrained at 2.5 $kcal.mol^{-1}.Å^2$, using a 1 fs integration timestep. Temperature was maintained using the Langevin thermostat with a collision frequency set to 1 $ps^{-1}$. Pressure equilibration MD simulations were then performed in semi-isotropic *(N, P, T)* ensemble in 5 steps in which PC polar head restraints were smoothly switched off as follow: (i) 125 ps, 1 $kcal.mol^{-1}.Å^2$, (ii) 500 ps, 0.5 $kcal.mol^{-1}.Å^2$, (iii) 500 ps, 0.1 $kcal.mol^{-1}.Å^2$, (iv) 500 ps, no restraints and (v) 1000 ps, no restraints, using a 2 fs integration timestep. Except for the last step, semi-isotropic Berendsen barostat was used to control pressure. Then, Montecarlo barostat was used for the last equilibration step as well as production runs of DPPC- and POPC-

LPC mixtures. Pressure was maintained using Berendsen barostat regarding pure Pl-Por bilayer membranes owing to the large deviation of box sizes occurring during equilibration from initially built systems. Production MD simulations were then carried at 298K, 1 atm for 1 and 2 μs respectively for mixture and pure LPC lipid bilayer membranes.

**Analysis.** Analyses were carried out over the last 500 ns of each run, ensuring stable equilibrated sampling. Most of the analyses were performed using the cpptraj and pytraj packages[33-34] from the Amber20 suite. C-atom lipid order parameters $S_{CD}$ were extrapolated from angles between C-H bonds and the bilayer normal[35]. Likewise, orientations of porphyrin were obtained using the angle $\theta$ between the lipid bilayer and the porphyrin core normal vectors. Order parameters were then obtained as follows[36]:

$$P_z = \frac{1}{2}\langle 3cos^2\theta - 1\rangle \quad \textit{(Eq. 1)}$$

Given that $\theta$ correspond to porphyrin core normal, order parameter values range from 1 to -0.5 respectively indicating that porphyrin core is aligned either to membrane plane or to lipid tails.

$\pi$-Stacking events were also calculated using similar approach used for H-bond analysis in cpptraj package. Briefly, for each porphyrin pair, inter-porphryin core distance and angle were calculated over MD simulations. It is worth mentioning that porphyrin core was hereby defined by the tetrapyrrole moiety only. Inter-porphyrin core angles were measured by calculating the angle between the vectors perpendicular to porphyrin cores. For each porphyrin pair, $\pi$-Stacking event was counted as 1 if both the inter-porphyrin core distance and angle were below 8.0 Å and 10°, respectively. For each pair of porphyrins, fractions were then obtained by summing the total count of $\pi$-stacking events over the number of frames considered during the analysis. Bilayer thicknesses and thicknesses maps were obtained based on the density of PC head P-atoms. Thickness maps were calculated on MD trajectories with 2Å resolution on the xy-plane, using

VMD Membplugin tool [37]. Thicknesses were then calculated by averaging thickness map values over the three replicas. Assessment of the packing parameter requires the accurate calculation of molecular volumes for porphyrin cores and sn1 lipid tail. However, such calculations are still relatively challenging for non-globular structures. Therefore, we here propose to assess packing parameters by measuring the projected distances between the porphyrin core and palmitic acid center-of-mass onto the xy-plane. By comparing these distances with the known PC cross sectional diameter extrapolated from cross sectional area parameter, it is thus possible to roughly estimate the shape of Pl-Por blocks. Molecular representations were rendered using the VMD-1.9.4-alpha package [38].

## RESULTS AND DISCUSSION

### Lipid-porphyrin conjugates synthesis

Starting from 1-lysophosphatidylcholine (C16, LPC) as lipid backbone, we synthesized six Pl-Por conjugates with increasing alkyl chain lengths in sn2 position and linked via a peptidic bond to either pheophorbide-a ($Ph_x$LPC) or pyropheophorbide-a ($Pyr_x$LPC) as porphyrinoid derivatives (Scheme 2). Due to the structural differences between the synthesized conjugates, it is expected that the PL-Por conjugates self-assemble into different supramolecular structures. In addition, reducing the length mismatch between the two chains would enable the formation of stable supramolecular assemblies. The major difference between the two porphyrinoids is the presence in pheophorbide-a of an extra methyl ester group in ortho position relative to the ketone functionality. This leads to a racemic mixture of two isomers in all conjugates containing Pheo-a. Firstly, the modified phospholipids were synthesized by conjugating the corresponding linker to the lysophosphatidylcholine backbone via a direct acylation of the carboxylate group and the secondary alcohol in sn2 position of the LPC. This acylation was carried out as reported

previously [24] following a modified procedure outlined by Rosetto et al [39-41]. In brief, the reaction mixture was sonicated at 25 °C in the presence of glass beads, under basic conditions using EDC.HCl to activate the carboxylic acid. Rosetto et al.[41] demonstrated that the incorporation of glass beads to the reaction is critical for the reaction to take place. They hypothesized that the glass beads under sonication transfer their kinetic energy to the reactants thus increasing the rate of this reaction and reducing the time from days to hours. It should be noticed that this reaction must be maintained at 25°C to avoid the intramolecular acyl migration which can occur at higher reaction temperatures. The resulting reactions gave three modified phospholipids (BocNH-Gly-LPC, BocNH-Ala-LPC and BocNH-γBuA-LPC) which were characterized by mass spectrometry and NMR. The three reactions provided a very good yield: 91% for BocNH-Gly-LPC, 87% for BocNH-Ala-LPC and 74% for BocNH-γBuA-LPC. Secondly, the amino group of each lipid was deprotected under acidic conditions using HCl and the deprotection was followed by the grafting of pheophorbide-a or pyropheophorbide-a. The PS attachment was carried out following a regular amide coupling reaction using EDC.HCl as coupling agent with HOBt under basic conditions. HOBt is usually used to improve peptidic coupling. The resulting procedure gave 6 different conjugates classified in two series: $Pyr_x$LPC was composed of $Pyr_2$LPC (yield 45%), $Pyr_3$LPC (yield 72%) and $Pyr_4$LPC (yield 44%). $Ph_x$LPC consisted of $Ph_2$LPC (yield 38%), $Ph_3$LPC (yield 42%) and the $Ph_4$LPC (yield 33%).

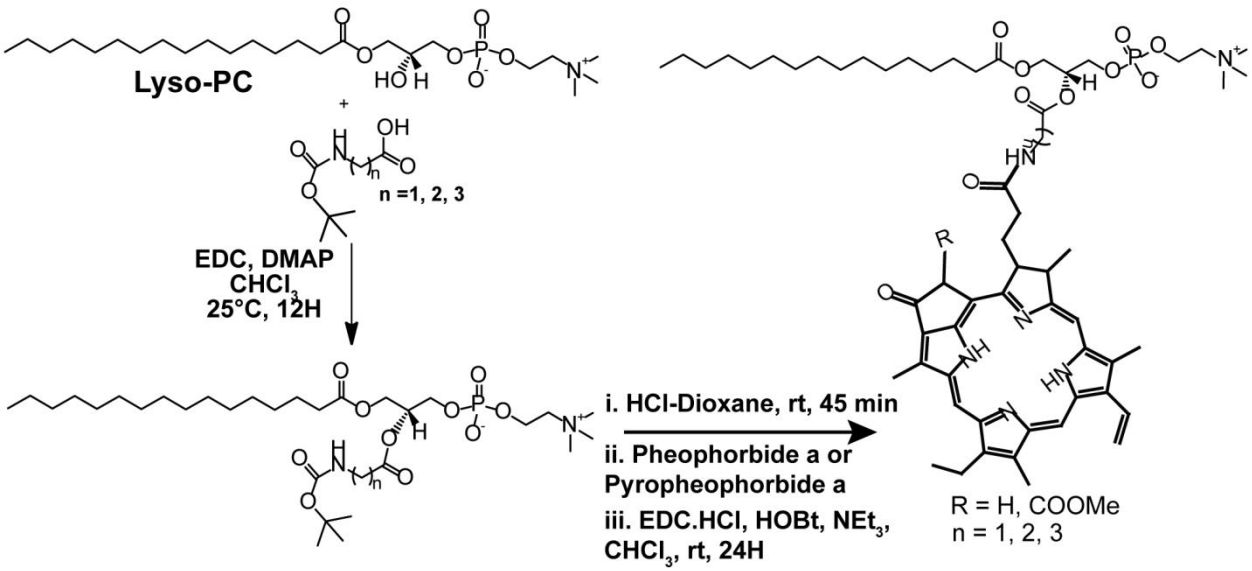


**Scheme 2.** Synthesis scheme of the studied lipid-porphyrin conjugates.

**Structural properties and optoelectronics of Pl-Por conjugate assemblies**

The self-assembling properties of the six synthesized lipid porphyrin conjugates were assessed by cryogenic transmission electron microscopy (cryo-TEM). The assemblies were made using the film hydration method followed by extrusion as usually done for liposomes preparation [24-25]. The addition of 2.5 mol % DSPE-$PEG_{2000}$ was necessary to avoid the aggregation of the conjugates and the loss of materials on the polycarbonate membrane during the extrusion step.

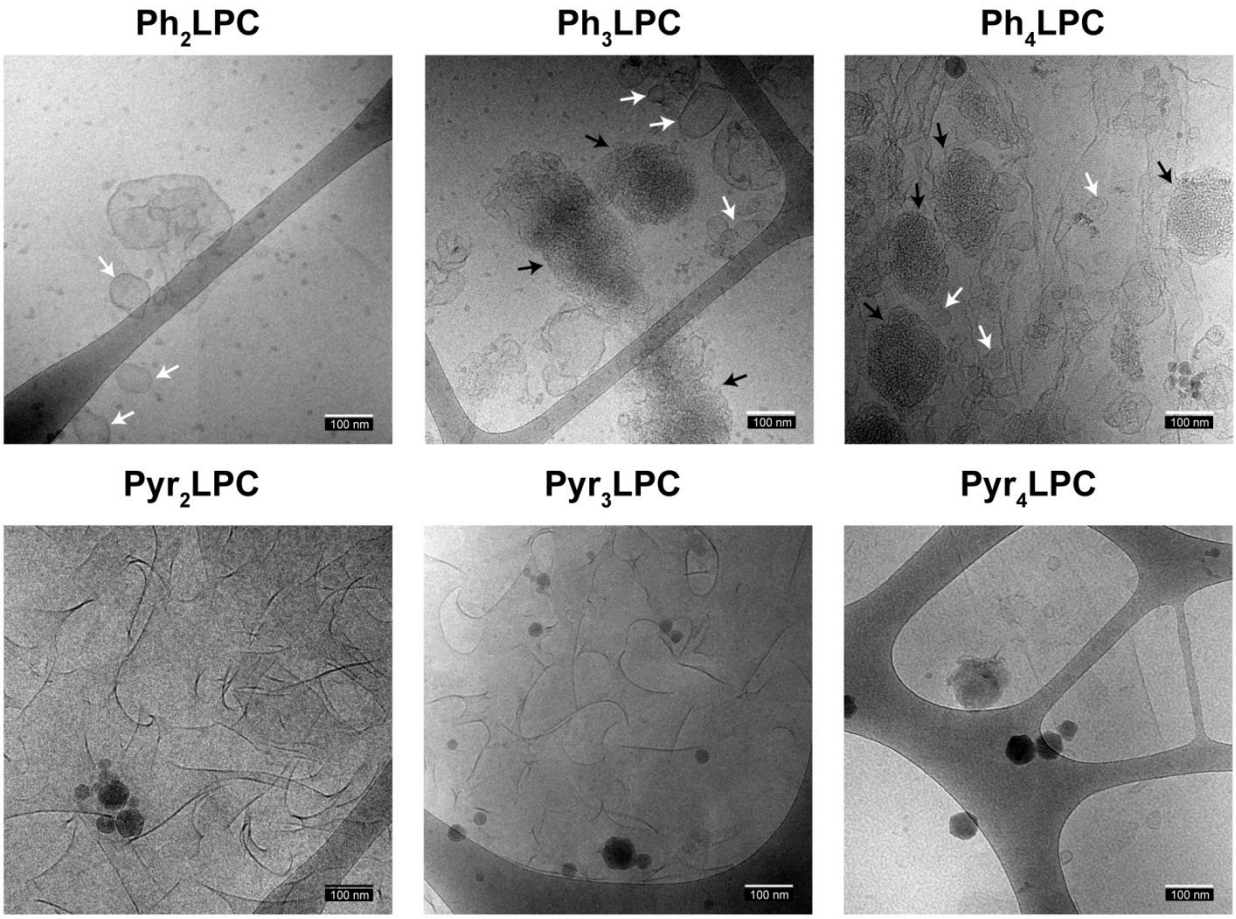


**Figure 1.** Cryo-electron micrographs of assemblies made of $Ph_xLPC$ and $Pyr_xLPC$ conjugates mixed with 2.5 mol % of DSPE-$PEG_{2000}$ in HEPES buffer.

As depicted in Figure 1, the six conjugates could form assemblies that are consistent with bilayers morphology. However, the cryo-TEM micrographs revealed a diversity in shapes depending not only on the nature of the photosensitizer (pheophorbide-a or pyropheophorbide-a) but also on the linker length between the lipid headgroup and the porphyrin. Whereas all $Ph_xLPC$ compounds formed unilamellar ovoid structures (white arrows) with the presence of spongious shapes (black arrows) for $Ph_3LPC$ and $Ph_4LPC$, $Pyr_xLPC$ assemblies exhibited open sheets morphology. The absorption and fluorescence of the various assemblies were recorded before and after their solubilization following the addition of organic solvents.

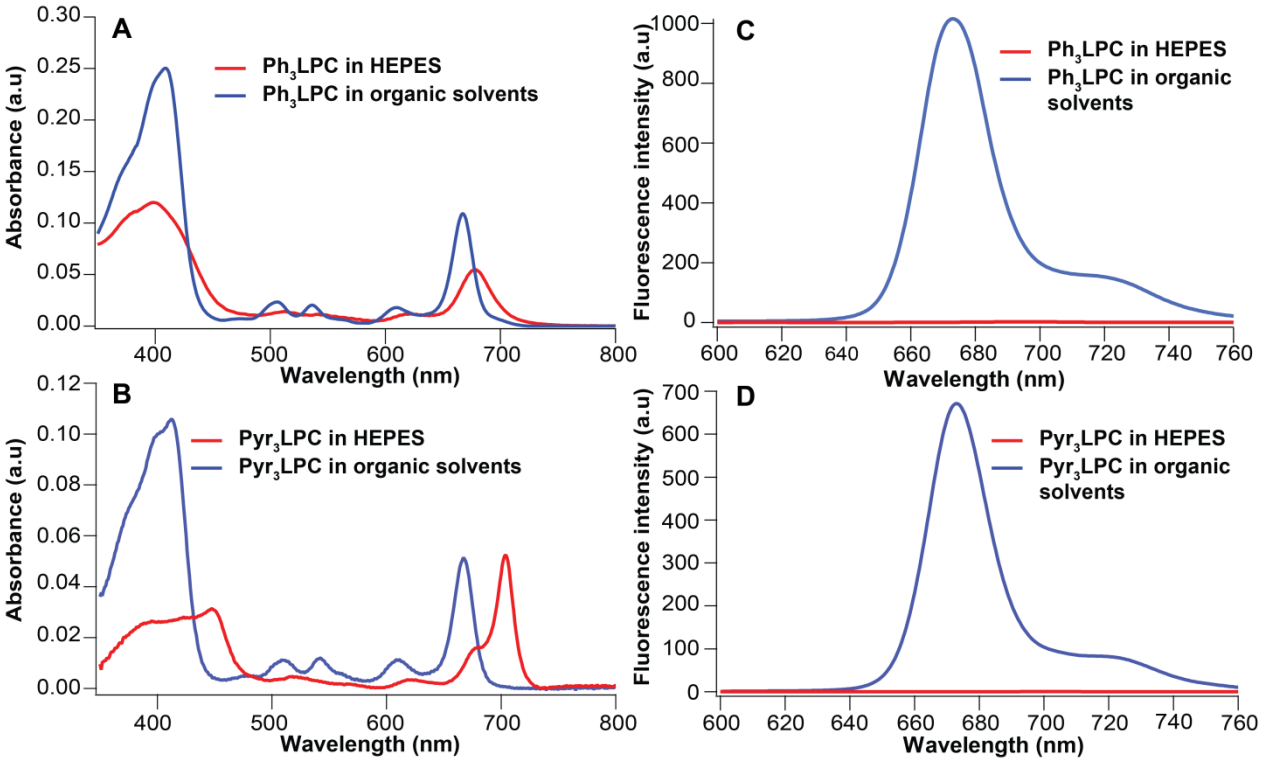


**Figure 2.** Absorbance and fluorescence spectra of $Ph_3LPC$-DSPE-$PEG_{2000}$ (A, C) and $Pyr_3LPC$-DSPE-$PEG_{2000}$ (B, D) assemblies, before (red line) and after (blue line) their solubilization in HEPES/MeOH/THF (0.2, 0.8, 1 mL) mixture.

As shown in Figure 2 and Figures S10-S11, the assemblies made of pure $Ph_xLPC$ or $Pyr_xLPC$ exhibit different absorbance features than their monomeric counterparts. In fact, while $Ph_xLPC$ assemblies exhibit a damping of the Soret and $Q_{max}$ bands with a light red shift (~12 nm) of this latter, the $Q_{max}$ of the $Pyr_xLPC$ conjugates is partially shifted from the monomer absorption at 667 nm to 703 nm with subsequent narrowing of this band. Such behavior corresponds to the formation of highly ordered porphyrin aggregates named J-aggregates [42-45] where porphyrin molecules are aligned in head to tail orientation [8, 23]. In such alignment, the lower energy excited states correspond to the states where the dipoles are in phase whereas the higher energy is forbidden. This results in a red-shifted and intensified absorption band of the assembly in comparison with the monomeric chromophores. This partial shift of the absorption band in

$Pyr_x$LPC nanoassemblies indicates that they are comprised of a mixed population of highly ordered and disordered porphyrin aggregates. Conversely, $Ph_x$LPC conjugates exhibit only disordered porphyrin aggregates. Both $Ph_x$LPC and $Pyr_x$LPC assemblies display extensively quenched fluorescence compared to the corresponding monomers released following solubilization (Figure 2, Figures S10 and S11). Similar behavior was observed previously by us [24, 46] and other groups [9, 23] but with other phospholipid-porphyrin conjugates and was related to the strong intermolecular interaction between the porphyrin molecules favored by the phospholipid-like structure of the conjugates.

**Insights into the supramolecular assembly of Pl-Por conjugates from MD simulations**

MD simulations were shown to be relevant to investigate supramolecular properties of conventional lipid bilayers [47] as well as those made of Pl-Por conjugates [22]. MD simulations were performed to get an atomic-scaled understanding about the structural influence of the different conjugates on the molecular organization, packing parameters of the conjugates, as well as on the driving forces. Each system was made of 128 $Ph_x$LPC or $Pyr_x$LPC molecules (Figure 3). Three replicas were run for 2 μs, each. MD simulations reveal structural differences between $Ph_x$LPC and $Pyr_x$LPC bilayers, as depicted by calculated thickness maps, averaged area per lipid (APL) and density profiles reported in Table 1 and Figure S21-23. For instance, the bilayers made of $Pyr_x$LPC are more ordered than $Ph_x$LPC ones, as shown by the calculated palmitate chain lipid order parameters ($S_{CD}$, see Figure 3B), regardless of the linker size. This is in line with calculated thicknesses which are slightly larger for $Pyr_x$LPC. Such result is also consistent with our recent monolayer study which showed that $Pyr_x$LPC conjugates form a film in the liquid-condensed state with subsequent appearance of well structured domains at the air/water interface [48].

**Table 1.** Pl-Por bilayer thickness (in Å), averaged area per lipid (APL, in Å) and lateral porphyrin-palmitate distance (in Å).

| | | Thickness (Å) | APL ($Å^2$) | Lateral porphyrin-palmitate distance (Å) |
|---|---|---|---|---|
| $Ph_xLPC$ | x = 2 | 36.8 ± 1.8 | 92.8 ± 0.4 | 13.2 ± 3.0 |
| | x = 3 | 34.4 ± 1.9 | 99.8 ± 1.6 | 12.2 ± 3.6 |
| | x = 4 | 37.6 ± 2.0 | 94.5 ± 1.6 | 9.6 ± 2.7 |
| $Pyr_xLPC$ | x = 2 | 38.8 ± 1.6 | 82.5 ± 0.7 | 12.7 ± 2.8 |
| | x = 3 | 38.0 ± 1.6 | 88.1 ± 1.4 | 11.8 ± 3.6 |
| | x = 4 | 39.9 ± 1.6 | 80.9 ± 0.4 | 8.9 ± 1.9 |

Likewise, the areas per lipid obtained for $Ph_xLPC$ systems are larger than those for the $Pyr_xLPC$ bilayers, regardless of the linker length. Interestingly, MD simulations reveal that $Ph_xLPC$ and $Pyr_xLPC$ molecules self-assemble to maximize dispersive interactions between porphyrin cores. Therefore, $Ph_xLPC$ and $Pyr_xLPC$ molecules are involved in a strong network of π-stacking interactions which lead to highly ordered supramolecular assemblies in agreement with aforementioned experimental observations. We quantified π-stacking events by using geometric criteria, namely (i) the distance between porphyrin cores and (ii) the angle between the two normal vectors of tetrapyrrole cores. π-stacking events were observed along simulations, for which the fractions of each porphyrin pair over time were calculated and summed in Figure 3C. It is worth mentioning that π-stacking interactions are sufficiently strong to be sometimes maintained for more than 70 % of simulations (see Table S1). Furthermore, MD simulations show two types of π-stacked dimers. On one hand, dimers are formed within the same leaflet in which dipole-dipole interactions are maximized by systematic structural shift between porphyrin cores along the stacking axis (Figure 3D).

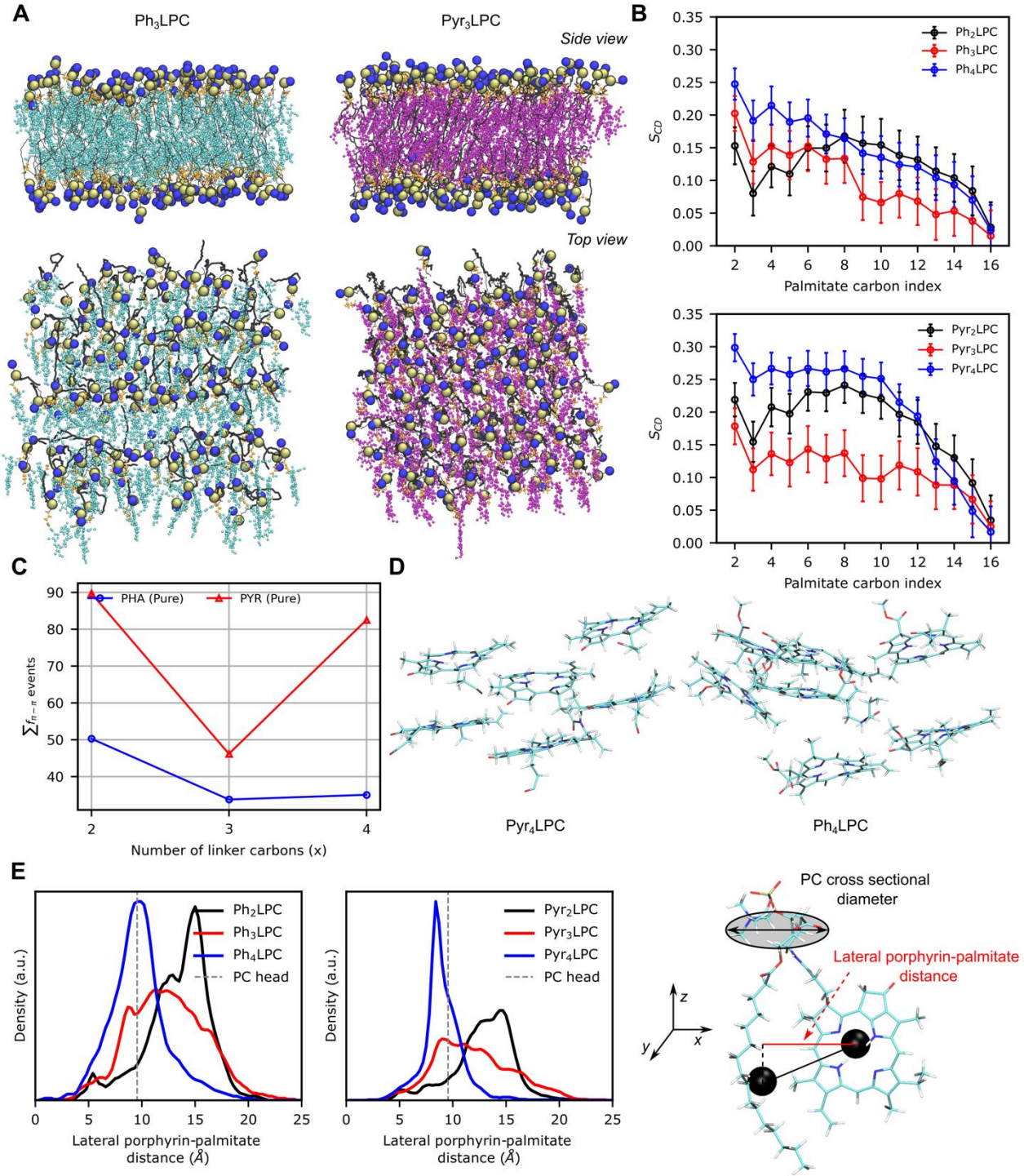


**Figure 3.** (A) Representative snapshots of self-assembled $Ph_3LPC$ (left) and $Pyr_3LPC$ into bilayers from MD simulations. Both side (top) and top (bottom) view are displayed. PC N- and P-atoms are depicted in blue and brown spheres, respectively. Pheo-a and Pyro-a porphyrin cores as well as palmitate chains and linkers are colored in cyan, purple, black and orange respectively. (B) Calculated lipid order parameters ($S_{CD}$) for palmitate carbons in $Ph_xLPC$ (top) and $Pyr_xLPC$ (bottom) simulations. (C) Overall sum of fractions of π-stacking events between porphyrin cores calculated along MD simulations and (D) representative snaphots (top view) of $Pyr_4LPC$ (left) and $Ph_4LPC$ (right) π-stacking organizations within

the Pl-Por bilayers. (E) Definition and distributions of lateral porphyrin-palmitate distance within Pl-Por bilayers for $Ph_xLPC$ (left) and $Pyr_xLPC$ (bottom). Later, porphyrin-PA distance was used to approximate the shape of porphyrin conjugates and compare to PC cross sectional diameter extrapolated from cross sectional area parameter.

On the other hand, inter-leaflet π-stacked dimers were also observed for which dipole-dipole interactions were maximized by adopting an anti-parallel conformation. This provides robust hints to rationalize the overall structural differences between $Ph_xLPC$ and $Pyr_xLPC$ bilayers. Indeed, regardless of linker size, $Ph_xLPC$ systems exhibit less π-stacking events with respect to $Pyr_xLPC$ ones (see Figure 3C). $Ph_xLPC$ molecules simply differ from $Pyr_xLPC$ by the presence of carboxymethyl moiety on porphyrin E-ring which is associated to a less planar porphyrin core. Furthermore, multiple stacking on both faces of porphyrin cores was not observed during simulations owing to the steric bulk arising from the axial orientation of carboxymethyl moiety in E-ring (see Figure 3D). Altogether, $Ph_xLPC$ self-assemble into less ordered lipid bilayers than $Pyr_xLPC$, as pictured by both experimental and computational results. This is in perfect agreement with the optoelectronics experiments where only pure $Pyr_xLPC$ molecules form J-aggregates. It is worth mentioning that the present MD simulations did not show the experimentally observed mixture of highly ordered and disordered porphyrin aggregates within Pl-Por bilayers. This is likely due to the limited size of modeled systems (128 lipids) and the relatively limited timescale (2 μs). This would require the modeling of much larger membranes by means of coarse-grained MD simulations.

MD simulations provided some hints about the role of linker size on the self-assembly of porphyrin conjugates. Even though such observations require further but challenging experimental validations, linker size seems to play a crucial role regarding π-stacking events. Indeed, both $Ph_3LPC$ and $Pyr_3LPC$ systems exhibit (i) less ordered bilayers (Figure 3B) and (ii)

less frequent π-stacking events (Figure 3C) compared to Pl-Por conjugates with either two or four carbon atoms in the linker. This highlights the balance between π-stacking driving forces and linker-driven porphyrin flexibility. The shortest linker may lead to more ordered Pl-Por bilayer owing to a lower flexibility of porphyrin core. Whereas the longest linker may be sufficiently flexible to favor proper stacking of porphyrin cores which in turn increase the structural order of the Pl-Por bilayer. The intermediate linker ($Ph_3$LPC and $Pyr_3$LPC) adopts then an intermediate behavior in which ideal π-stacking is more difficult to obtain, because the linker is too short but sufficiently long to allow enough flexibility to the porphyrin.

Lateral porphyrin-palmitate distances were calculated as an approximation of packing parameters (Figure 3E). Both porphyrin conjugates exhibit similar behavior. Taking into account these results and assuming that PC headgroup cross section diameter is 9.71 Å [49], $Pyr_2$LPC and $Ph_2$LPC should adopt slightly negative curvature, owing to the lower flexibility of the linker. Moreover, MD simulations suggest that porphyrin conjugates with the longer linker tend to adopt a planar curvature since the ratio between lateral porphyrin-palmitate distance and PC head cross section diameter are close to 1, which is particularly true for $Pyr_4$LPC and $Ph_4$LPC systems. However, the cryo-TEM results revealed that all Pl-Por conjugates assemble into bilayers. This demonstrates that the calculation of the packing parameter is not sufficient to predict assembly of the Pl-Por conjugates given their shapes in contrast to conventional phospholipids and detergents. Such findings highlight that the interactions between porphyrin cores plays a central role in controlling both the structure of the lipid bilayer membranes and their optical properties.

**Thermotropic phase behavior of lipid bilayers incorporating Pl-Por conjugates**

Although $Ph_xLPC$ and $Pyr_xLPC$ could self-assemble into bilayers, only few structures that resemble to vesicles were observed. Thus it was important to determine if these conjugates could be embedded into a liposomal bilayers made of conventional phospholipids while maintaining their optical properties (i.e., J-aggregates and fluorescence quenching properties). To do so, we prepared DPPC lamellar suspensions incorporating 1 to 10 mol % of either $Ph_xLPC$ or $Pyr_xLPC$, and we studied their thermotropic behavior using differential scanning calorimetry (DSC). As shown in Figure 4, pure DPPC lamellar phases exhibit the typical thermal behavior of DPPC bilayers [50-52] with a broad peak at 33.8°C corresponding to the pretransition from the gel ($L_{\beta'}$) to the ripple phase ($P_{\beta'}$) and a sharp and intense peak at 41.2°C assigned to the main $P_{\beta'}/L_{\alpha}$ phase transition. The incorporation of Pheo-a seems to impact slightly the thermal behavior of these bilayers (Figure S12). Indeed, up to 5 mol % Pheo-a the pretransition phase remains and there is only a slight broadening of the main transition peak which maintains its symmetrical shape even at 10 mol %. This suggests that the Pheo-a molecules are not incorporated deeply in the DPPC matrix. Similar behavior is observed for $Ph_xLPC$ conjugates up to 2.5 mol %. However, from 5 mol % the pretransition phase vanishes and the main transition peak becomes broader with an asymmetrical shape. Taken together, these results demonstrate that $Ph_xLPC$ compounds can insert deeper than Pheo-a in the DPPC matrix due to their resemblance to phospholipids, and they perturb to a higher extent the intermolecular cooperativity between DPPC molecules, however without causing phase separation in the lipid matrix.

Although the thermograms of DPPC bilayers incorporating Pyro-a are similar as those obtained with Pheo-a (Figure S12), it is clear that the $Pyr_xLPC$ molecules alter significantly more the thermal behavior of DPPC than $Ph_xLPC$ ones. As their concentration increases, $Pyr_xLPC$ molecules induce a broadening of the main transition peak, a significant shift of the $T_{onset}$ of the

main transition towards lower temperatures and the appearance of a second peak/shoulder at lower temperature for mixtures with $Pyr_x$LPC higher than 2.5 mol %. In addition, the weight balance between the first and the second peak is impacted as the mol % of $Pyr_x$LPC rises from 5 to 10 mol %; whereas the first peak corresponding to the new phase increases, the second peak decreases. Hence independently from the chain length, these findings indicate the formation of a second phase which is governed by the concentration of $Pyr_x$LPC incorporated into the DPPC bilayer. This implies that $Pyr_x$LPC conjugates have the tendency to phase separate from DPPC by forming $Pyr_x$LPC rich domains in the DPPC bilayer.

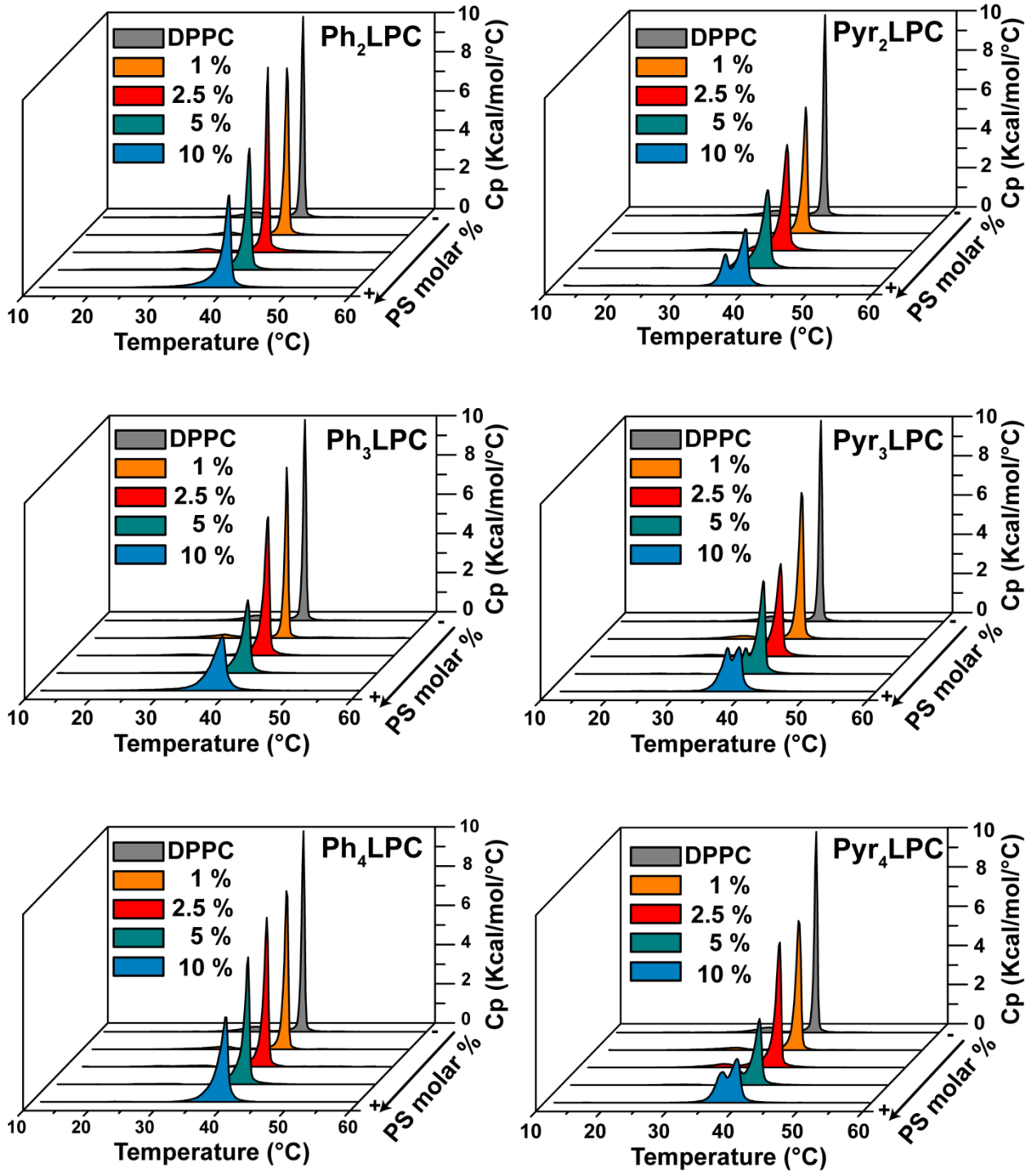


**Figure 4.** DSC heating scans for DPPC lamellar suspensions incorporating increasing molar percentages (1-10 mol %) of $Ph_xLPC$ (left column) or $Pyr_xLPC$ (right column).

**Optoelectronic properties of liposomes incorporating Pl-Por conjugates**

To assess if the incorporated $Ph_xLPC$ and $Pyr_xLPC$ in DPPC bilayers maintain their optical properties as the pure compounds, DPPC liposomes with various mol % of $Ph_xLPC$ or $Pyr_xLPC$ were prepared.

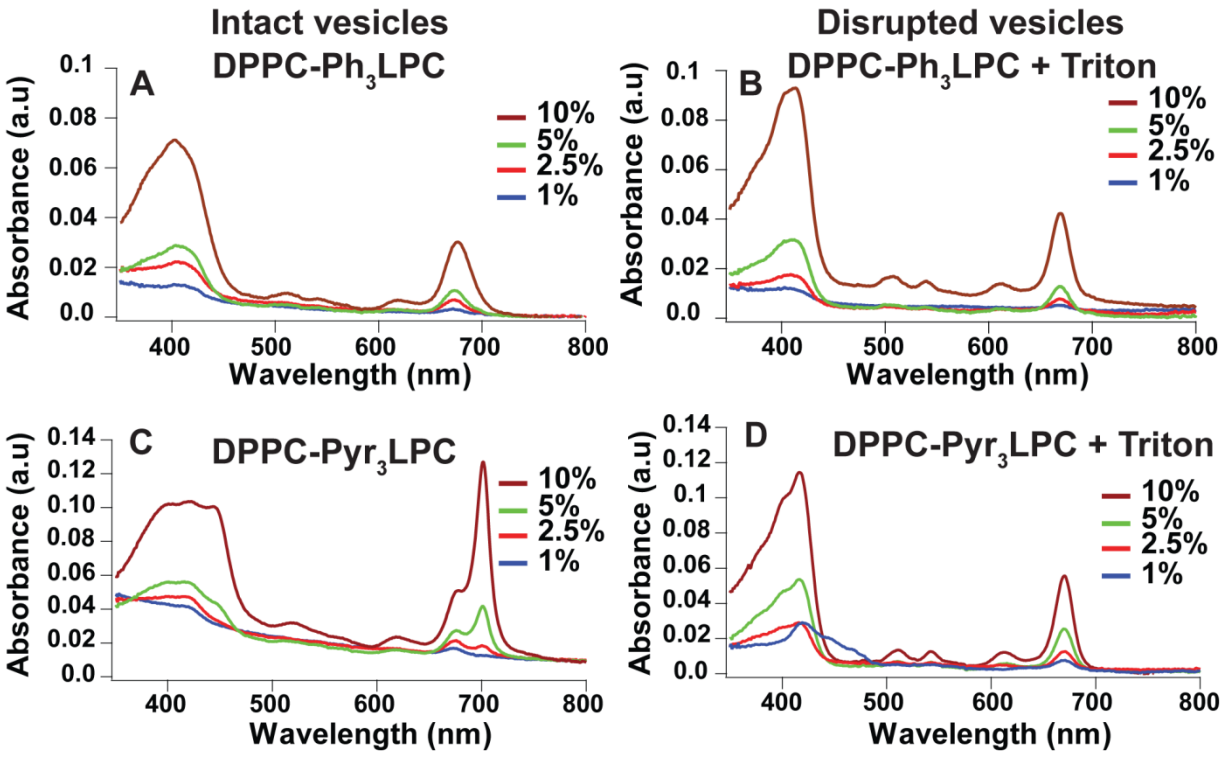


**Figure 5.** Absorbance spectra of DPPC assemblies incorporating different molar percentage (1-10 mol %) of either $Ph_3LPC$ (A, B) or $Pyr_3LPC$ (C, D), before (A, C) and after (B, D) their disruption by adding Triton X-100 (1 % V/V).

As for the pure Pl-Por assemblies, fluorescence quenching is observed for all DPPC/Pl-Por formulations (Figure S13-S15). Moreover, the fluorescence quenching becomes more intense as the molar percentage of Pl-Por conjugates in the DPPC bilayer increases (Figure S13-S15). Figure 5 compares the absorption spectra for DPPC-$Ph_3LPC$ and DPPC-$Pyr_3LPC$ assemblies. Interestingly, both of them exhibit similar optical behavior as the assemblies made of the pure conjugates. Whereas the absorbance spectra of liposomes containing $Ph_3LPC$ display a

broadening of the $Q_{max}$ band with a slight red shift, those incorporating $Pyr_3$LPC exhibit significant red shift with subsequent sharpening of the new Q band at 703 nm. In addition, the weight balance $Q_{703nm}/Q_{667nm}$ increases linearly with the mol % of $Pyr_3$LPC. This demonstrates that the higher the $Pyr_x$LPC concentration in the DPPC bilayer, the more likely the formation of J-aggregates in the bilayer due to the proximity of porphyrin molecules. The same difference in behavior was observed for the other $Ph_x$LPC and $Pyr_x$LPC conjugates independently of the linker length (Figures S16-S17). This demonstrates that the porphyrin structure rather than the linker length dictates the formation of the J-aggregates.

This result is consistent with the DSC experiments that indicated a phase separation in the DPPC bilayers with $Pyr_x$LPC content higher than 2.5 mol%, independently of their linker length. It is noteworthy, however, that although the J-aggregates band increases, the band corresponding to the monomeric Pl-Por is still present (Figure 5). This implies that the formation of J-aggregates is only partial. Similar results have been obtained by Charron et al.[23] with bacteriopheophorbide-a PS linked via an ester bond to a 1-lysophosphatidylcholine. By measuring the absorption spectra as function of the temperature and DPH fluorescence anisotropy on DSPC/Lipid-Por (85/15 mol %), they could demonstrate the phase separation of the Pl-Por conjugates into J-aggregates with the presence of minor population of disordered aggregates that were photodynamically active despite the high fluorescence quenching [23].

**Cryo-TEM analysis of the morphology of liposomes incorporating Pl-Por conjugates**

Using Cryo-TEM, we analyzed the morphology of DPPC liposomes doped with $Ph_x$LPC or $Pyr_x$LPC at 2.5 and 10 mol %. Figure 6 shows that all DPPC/$Ph_x$LPC mixtures form semi-spherical unilamellar vesicles independently of the mol % or the length of the linker in $Ph_x$LPC (i.e. x = 2, 3 or 4). It is worth noting, however, that the liposome membranes are not smooth but

display several membrane fluctuations or undulations, and this phenomenon becomes particularly visible at high $Ph_xLPC$ molar percentage. Such observation implies the formation of different local curvatures that may be due to the segregation of $Ph_xLPC$ into disordered membrane areas between highly ordered DPPC domains. Similar shapes have been observed by Ickenstein et al. [53] for DPPC vesicles incorporating micelle-forming membrane components such as lysolipids and polyethyleneglycol-conjugated lipids (PEG-lipids).

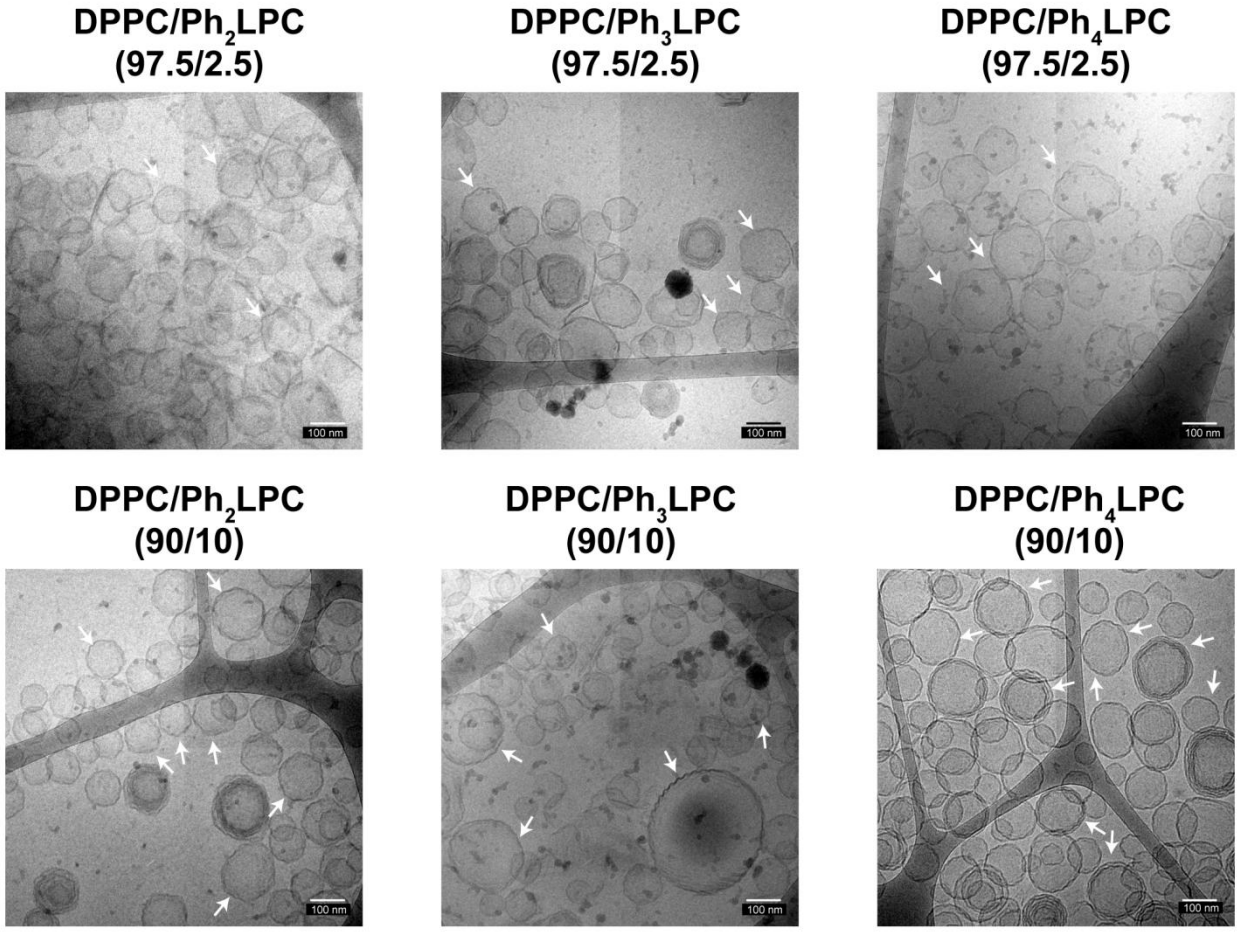


**Figure 6.** Cryo-electron micrographs of DPPC vesicles incorporating either 2.5 or 10 mol % of $Ph_xLPC$ conjugates in HEPES buffer. White arrows indicate some structures presenting membrane undulations or fluctuations.

For DPPC-$Pyr_xLPC$ liposomes, different structures were observed depending on the molar percentage of the incorporated lipid-porphyrin conjugates and the linker length (Figure 7). At 2.5 mol%, DPPC-$Pyr_xLPC$ liposomes were mostly spherical vesicles exhibiting either smooth

membrane or undulations. When the molar percentage increased to 10 mol%, the assemblies showed different structures depending on the $Pyr_x$LPC conjugate. Indeed, while the cryo-electron micrographs of DPPC-$Pyr_2$LPC assemblies revealed faceted structures and vesicles with undulated membranes, DPPC-$Pyr_3$LPC and DPPC-$Pyr_4$LPC exhibited tubular and facetted polyhedral vesicles with sharp edges, respectively (Figure 7). To form such faceted structures, there must be an underlying mechanism that increases the energy cost associated with the shell (i.e. bilayer) bending [54-55]. Previous works on multicomponent elastic shells [56] or faceted lipid vesicles [57] have reported that the formation of faceted structures is related to the phase separation between two incompatible components into two regions where liquid-like edges separate flat crystalline domains to decrease the strain energy imposed by the crystalline phase. Thus, such faceted structures are formed by a combination of line tension and the relative bending rigidities difference between the two components.

As seen in the Cryo-TEM micrographs of pure $Pyr_x$LPC (Figure 1), these components can assemble into open rigid sheets. When incorporating the conjugates in DPPC bilayers they segregate to form hard regions with higher bending rigidity compared to that of pure DPPC bilayer. Thus, the soft DPPC regions will bend and separate the hard flat facets formed in $Pyr_x$LPC rich regions. This interpretation is further supported by the DSC results and the absorption spectra that indicate the phase separation and the formation of J-aggregates with the increasing amount of $Pyr_x$LPC in DPPC bilayers.

Further evidence was provided about the correlation between the formation of the facets and the segregation of $Pyr_x$LPC into J-aggregates by incorporating the Pl-Por conjugate at a molar percentage of 10 % into POPC liposomes. Indeed, POPC molecules form less ordered bilayers than DPPC ones due to their much lower phase transition temperature, and this should limit the segregation of the $Pyr_x$LPC molecules. As shown in Figure S18, the absorption spectra of POPC-

$Pyr_xLPC$ do not show the Q-band of the J-aggregates. Moreover, the Cryo-TEM micrographs of the POPC-$Pyr_xLPC$ liposomes in Figure S19 reveal spherical vesicles with a smooth bilayer. Interestingly, heating the liposomes made of DPPC-$Pyr_3LPC$ and those made with phospholipids with higher melting temperatures such as DSPC and DAPC revealed the disappearance of the Q band of the J-aggregates at temperatures exceeding the melting temperature of the bilayer (Figure S20). Taken together, these results suggest that the fluidity of the phospholipid bilayer controls whether J-aggregates of $Pyr_xLPC$ can be formed or not. Similar behavior was observed by Gang Zheng's group [23] who demonstrated that J-aggregates of bacteriopheophorbide-a coupled to 1-lysophosphatidylcholine via an ester bond can be formed in saturated DSPC bilayers even at low molar percentage (1-15 mol %), while in the unsaturated DOPC bilayer only disordered aggregates are detected.

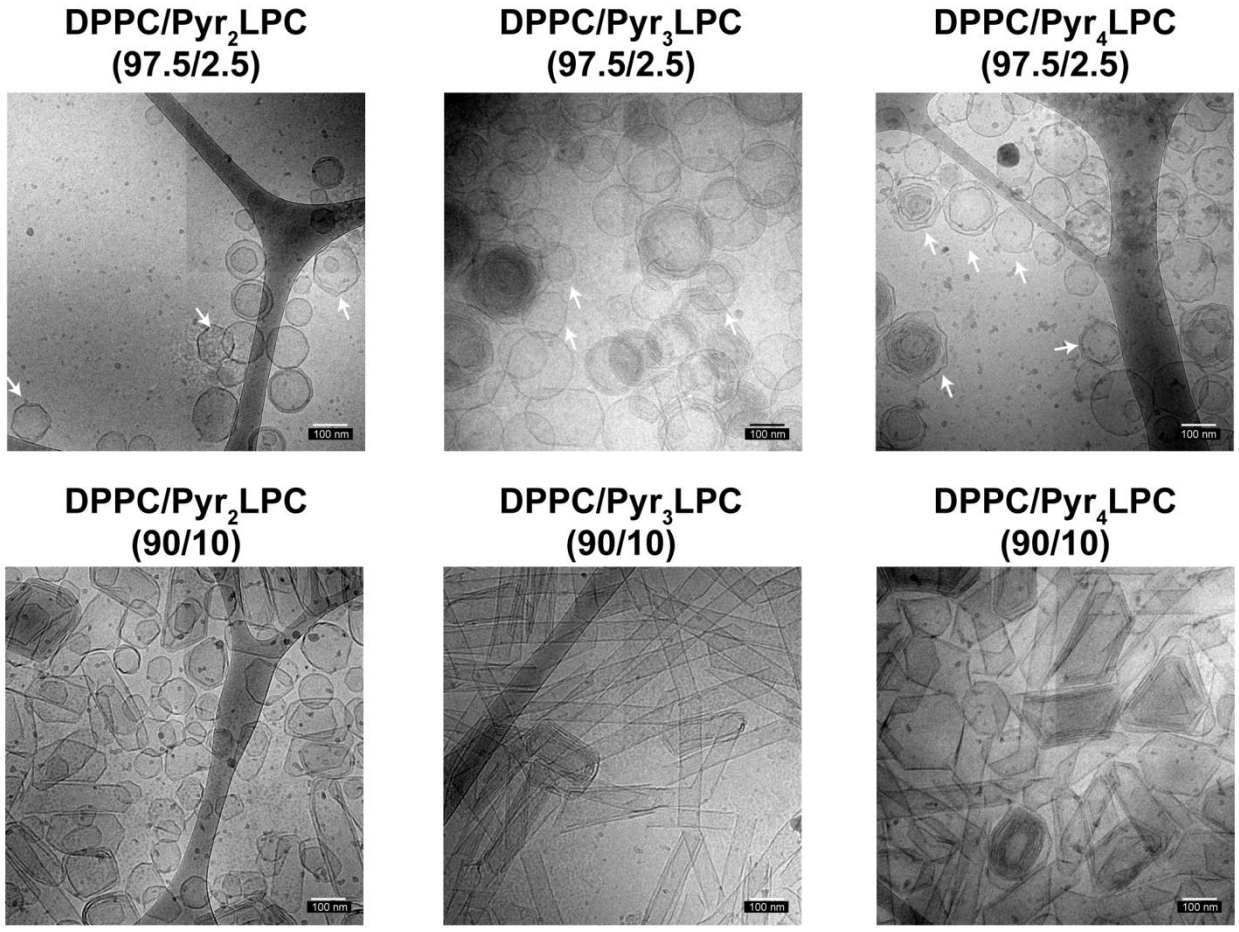


**Figure 7.** Cryo-electron micrographs (Cryo-TEM) of DPPC vesicles incorporating either 2.5 or 10 mol % of $Pyr_x$LPC conjugates in HEPES buffer.

**Atomic-scaled structures of DPPC and POPC bilayers incorporating Pl-Por conjugates**

To get a better understanding of the experimental observations, DPPC-$Ph_x$LPC, DPPC-$Pyr_x$LPC, POPC-$Ph_x$LPC and POPC-$Pyr_x$LPC systems were investigated by means of MD simulations considering either 2.5 mol % or 10 mol % of Pl-Por. DPPC bilayers doped with Pl-Por conjugates exhibit the typical structural behavior of DPPC gel phase given that simulations were performed at T = 25°C (Figure 8A). The calculated thicknesses and the APL (Table 2, Figures S24-S27) are in line with experiments and previous studies in which *e.g.*, the APL of DPPC was shown to be *ca.* 48 $Å^2$ and the thickness ranged from 47 to 55 Å [58-59]. Lipid tail order $S_{CD}$ parameters were

also computed supporting the gel and liquid phase of DPPC- and POPC-based lipid bilayer membranes (Figures S29-S30).

In all simulations, Pl-Por conjugates partition in the lipid bilayer membrane, regardless of their concentration (see Table 2). This agrees with the aforementioned experiments except for the incorporation of $Ph_xLPC$ compounds in DPPC lipid bilayer membranes at 2.5% mol. This is explained by the computational setup for which Pl-Por conjugates were directly all incorporated in a DPPC lipid bilayer membrane. Thereby, joint computational and experimental investigations suggest that, at low concentration, $Ph_xLPC$ is kinetically less likely to insert into the DPPC lipid bilayer membrane with respect to $Pyr_xLPC$, owing to the presence of polar carboxymethyl moiety. This chemical group may increase (i) the dipole moment of porphyrin core and/or (ii) the steric hindrance while penetrating in ordered lipid bilayer membrane. The latter is strongly supported by (i) POPC-experiments in which Pl-Por conjugates partition in the lipid bilayer membrane regardless of the Pl-Por type and (ii) the expected higher energy cost to insert in DPPC rather than in POPC, as suggested by recent computational investigations [60-61].

**Table 2.** Lipid bilayer thickness based on distance between P-atom density peaks (in Å), averaged area per lipid (APL, in $Å^2$) and averaged distances of porphyrin core with respect to lipid bilayer membrane center of mass (dz, in Å) for DPPC- and POPC- $Ph_xLPC$ and -$Pyr_xLPC$ systems

| % mol | | | DPPC/PL-Por | | | POPC/PL-Por | | |
|---|---|---|---|---|---|---|---|---|
| | | | Thickness (Å) | APL ($Å^2$) | $d_z$ (Å) | Thickness (Å) | APL ($Å^2$) | $d_z$ (Å) |
| 2.5 % | $Ph_xLPC$ | x = 2 | 46.7 ± 3.7 | 45.8 ± 1.2 | 10.1 ± 6.0 | 39.8 ± 2.0 | 62.2 ± 1.0 | 11.3 ± 2.7 |
| | | x = 3 | 46.7 ± 3.7 | 45.9 ± 1.6 | 7.3 ± 5.8 | 39.6 ± 1.9 | 62.4 ± 0.9 | 11.3 ± 2.8 |
| | | x = 4 | 47.3 ± 3.6 | 45.3 ± 0.7 | 10.6 ± 5.5 | 39.6 ± 1.9 | 62.7 ± 1.0 | 11.2 ± 2.7 |
| | $Pyr_xLPC$ | x = 2 | 48.2 ± 3.4 | 44.3 ± 1.0 | 11.7 ± 6.0 | 39.9 ± 2.0 | 61.9 ± 1.0 | 11.0 ± 2.7 |
| | | x = 3 | 48.2 ± 3.3 | 44.3 ± 0.5 | 9.9 ± 6.0 | 39.8 ± 1.9 | 61.9 ± 1.0 | 10.6 ± 2.8 |
| | | x = 4 | 48.2 ± 3.4 | 44.1 ± 0.7 | 10.6 ± 6.1 | 39.8 ± 1.9 | 62.1 ± 0.9 | 10.8 ± 2.6 |
| 10 % | $Ph_xLPC$ | x = 2 | 46.5 ± 3.8 | 49.2 ± 0.6 | 10.3 ± 6.2 | 40.0 ± 1.9 | 63.7 ± 0.9 | 10.8 ± 3.6 |

| | | | | | | | |
|---|---|---|---|---|---|---|---|
| | x = 3 | 46.0 ± 3.9 | 49.9 ± 0.8 | 9.0 ± 5.0 | 39.8 ± 2.2 | 64.3 ± 0.9 | 9.5 ± 4.0 |
| | x = 4 | 45.8 ± 4.1 | 50.2 ± 0.7 | 8.8 ± 4.9 | 39.7 ± 1.9 | 64.5 ± 1.0 | 10.3 ± 3.6 |
| $Pyr_x$LPC | x = 2 | 47.2 ± 3.3 | 47.7 ± 0.6 | 10.5 ± 5.4 | 40.7 ± 1.9 | 61.9 ± 0.9 | 11.1 ± 2.8 |
| | x = 3 | 46.6 ± 4.0 | 48.7 ± 1.1 | 9.9 ± 5.7 | 40.2 ± 2.2 | 62.6 ± 0.9 | 10.8 ± 2.9 |
| | x = 4 | 47.0 ± 3.2 | 48.2 ± 0.6 | 10.6 ± 5.3 | 40.3 ± 1.9 | 63.1 ± 1.0 | 11.3 ± 3.2 |

Interestingly, MD simulations strongly support the importance of Pl-Por structure and concentration. $Ph_x$LPC at 10 mol % concentration are more likely to modify DPPC bilayer structure than at 2.5 mol %. For instance, calculated thickness maps revealed local bilayer deformations for which thickness shrinking events are more pronounced at 10 mol % than 2.5 mol % (Figure S24). In contrast, the presence of $Pyr_x$LPC molecules is expected to have a lesser effect on DPPC lipid bilayer, even locally. This might be explained by the inter-leaflet interactions between porphyrin cores of $Ph_x$LPC compounds. Experiments suggested that DPPC/$Pyr_x$LPC systems undergo phase separation events for concentration higher than 2.5 mol %. Unfortunately, this was not observed in MD simulations owing to the limited μs-timescale. Indeed, phase separation is driven by phenomena for which timescales range from dozen of microseconds to seconds [62] which require the use of coarse-grained MD simulations. However, present simulations provide robust hints about plausible underlying mechanisms which might ultimately lead to phase separation events.

Simulations performed with POPC bilayer show that lipid bilayer membranes are almost not impacted by the incorporation of Pl-Por conjugates, regardless of the concentration (Table 2 and Figures S26-27). This supports the experimental findings where the fluidity of lipid bilayer membrane seemed to govern the dynamic behavior of the Pl-Por conjugates, rather than the porphyrin core structure or the linker length. This is further confirmed by assessing the distribution function of porphyrin depths of insertion in the lipid bilayers (see Figure S32).

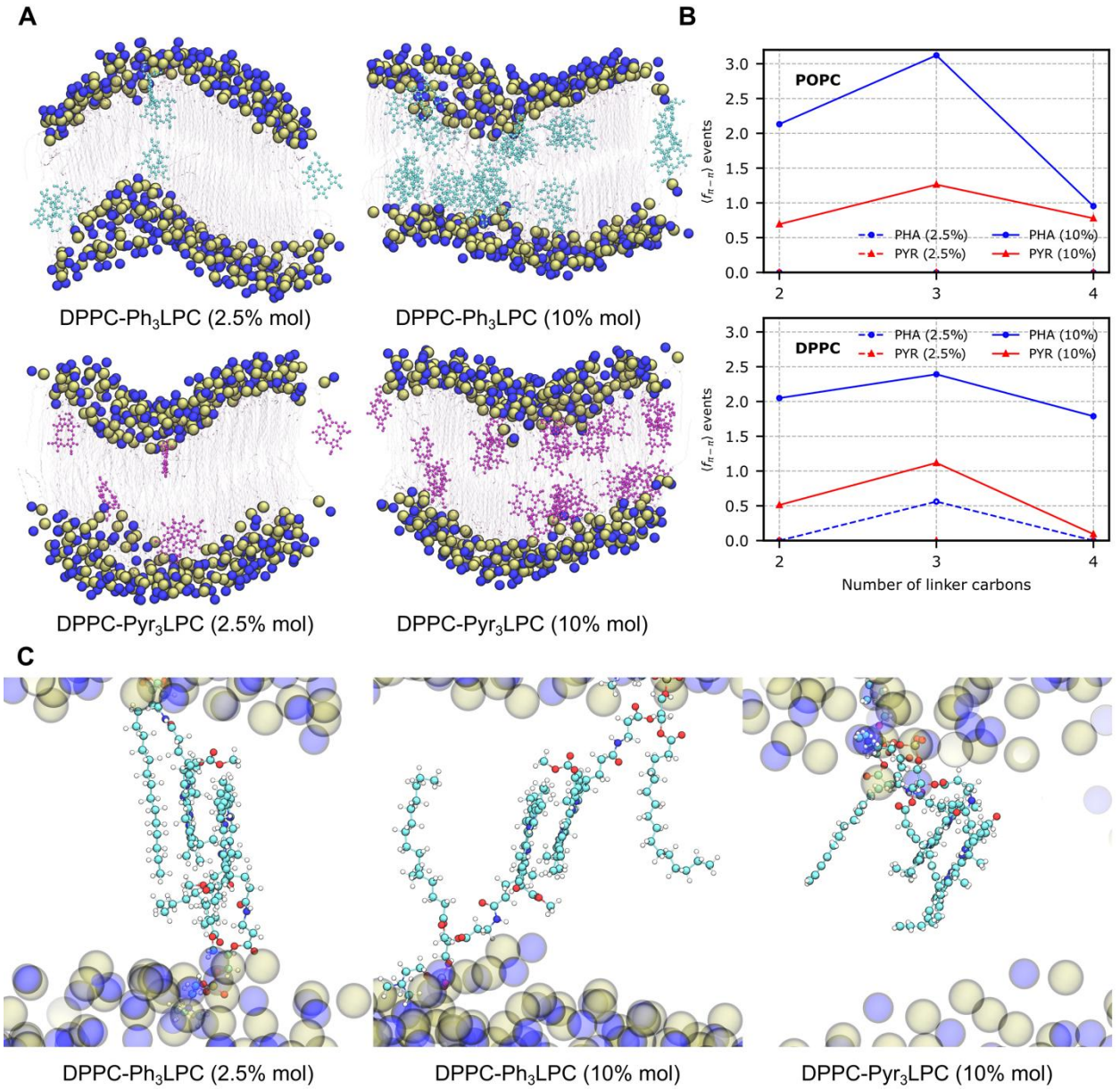


**Figure 8.** (A) Representative snapshots of DPPC-$Ph_3$LPC (top) and DPPC-$Pyr_3$LPC system from MD simulations. PC N- and P-atoms are depicted in blue and brown spheres, respectively. $Ph_3$LPC and $Pyr_3$LPC porphyrin cores as well as palmitate chains and linkers are colored in cyan, purple, orange and black. (C) Overall sum of π-stacking event fractions for all DPPC- and POPC-LPC systems. (C) Representative examples of DPPC-$Ph_3$LPC (left: 2.5 mol % and center: 10 mol %) and DPPC-$Pyr_3$LPC (right: 10 mol %) π-stacked conformations, highlighting inter-leaflet and intra-leaflet events respectively for $Ph_3$LPC and $Pyr_3$LPC.

While average distances of porphyrin core with respect to lipid bilayer membrane center-of-mass (COM) does not exhibit significant differences between the different lipid bilayer compositions,

the distribution function reveals that porphyrin cores are more likely to move in fluid POPC bilayers than in DPPC-based bilayers. The more ordered the lipid bilayer membrane, the more localized the depth of penetration. Porphyrin orientations within a lipid bilayer were also investigated suggesting that the porphyrin moieties lay along the lipid tails as pictured by the calculation of order parameters $P_z$ (see Figure S31).

**Rationalizing non-covalent interactions of Pl-Por conjugates when incorporated in DPPC or POPC bilayers**

To rationalize the formation of J-aggregates within DPPC lipid bilayer, inter-porphyrin π-stacking events were monitored along MD simulations of DPPC and POPC bilayers doped with Pl-Por conjugates (see Figure 8B and Table S1). In agreement with experimental observations made on J-aggregate formation, the higher the content of Pl-Por incorporated in DPPC bilayers, the more likely the π-stacking between porphyrin cores. However, the calculated π-stacking fractions remain low considering the number of porphyrin cores. This is consistent with the absorbance results since J-aggregate formation was shown to be only partial (Figure 5 and 8A). However, the use of calculated π-stacking fractions alone is not sufficient to rationalize the experimentally observed difference between POPC and DPPC vesicles containing $Pyr_x$LPC at 10 mol %. Indeed, while the calculated π-stacking fractions remain in the same order of magnitude (*e.g.*, 1.263 and 1.117 for POPC- and DPPC-$Pyr_3$LPC, respectively, see Table S1), optical experiments revealed the absence of J-aggregate Q-bands in the former. Interestingly, the number of porphyrin pairs involved in π-stacking events is systematically larger for POPC-based lipid bilayer membranes than for DPPC ones. In other words, a similar number of π-stacking events is observed in both POPC and DPPC bilayers incorporating 10 mol % of Pl-Por but more

porphyrins are involved in the former. This strongly suggests that π-stacked conformation lifetime is lower in POPC than in DPPC. J-aggregates are thus expected to be formed in POPC but for a significantly lower lifetime which may explain the absence of J-aggregate Q-band in the experiments. Both experiments and MD simulations suggest that more ordered DPPC bilayers are likely to decrease the diffusion of Pl-Por with respect to POPC, which in turn increases π-stacked conformation lifetime.

Finally, particular attention was paid to the interplay between the conformation of π-stacked dimers and the structure of a porphyrin core. Interestingly, when incorporated in DPPC bilayer at 10 mol %, $Ph_x$LPC compounds favor the formation of inter-leaflet dimers (Figure 8C), while $Pyr_x$LPC dimers are mostly observed within the same leaflet. For instance, up to 73% of observed π-stacked dimers involved both leaflet for $Ph_x$LPC (see Table S1). This could be related to the structural differences between the two porphyrin moieties. Indeed, the absence of bulky E-ring carboxymethyl moiety in $Pyr_x$LPC system favors the formation of π-stacked dimers, regardless of which porphyrin face interacts with another porphyrin (*i.e.*, *Si/Re*-like, see Figure 8A). In contrast, the presence of carboxymethyl moiety in $Ph_x$LPC core (i) sterically decreases the likelihood of intra-leaflet π-stacked dimers and (ii) increases the dipole moment. Both events favor the formation of inter-leaflet anti-parallel π-stacked dimers. The presence of inter-leaflet dimers leads to strong local deformation of DPPC lipid bilayer membrane in which *e.g.,* thickness is lower (as pictured in Table 2 and Figure 8A). This is further supported by the membrane undulations and fluctuations observed in the cryo-TEM experiments. Finally, DPPC-$Pyr_x$LPC simulations can shed light on the underlying mechanism for the suggested phase separation observed in both DSC thermodynamics and cryo-TEM experiments. Indeed, MD simulations showed that $Pyr_x$LPC cores can π-stack regardless of Si/Re arrangement. Therefore, it is likely

that more than two $Pyr_x$LPC partners can stack upon time. This event may be considered as a self-assembly nucleation event. It is worth mentioning that this event is expected to be controlled by the lateral diffusion of $Pyr_x$LPC for which the size of the linker is likely to play a role. This might then explain the difference observed between the DPPC-$Pyr_x$LPC vesicles.

## CONCLUSIONS

Pl-Por conjugates are versatile molecules that can self-assemble into supramolecular structures while exhibiting unique multifunctional properties. However, the driving forces behind their assembly remain unclear. Owing to their structural similarities with phospholipids, we expected that the shape and the morphology of the Pl-Por conjugates self-assembled structures could be simply predicted from the calculation of their geometric packing parameters. Hence, six new Pl-Por conjugates possessing various geometrical packing parameters were synthesized. The new $Ph_x$LPC and $Pyr_x$LPC conjugates exhibit different linker lengths in sn2 position and bear either Pheo-a or Pyro-a at the linker extremity, respectively. It was thought that changing the linker length between the polar headgroup and the porphyrin core may modulate the chain length mismatch between the sn1 and sn2 chains and thus dictate the morphological structures of the assemblies. Both $Ph_x$LPC and $Pyr_x$LPC were able to self-assemble into supramolecular structures consistent with bilayers morphology and exhibiting different optoelectronic properties that were not dependent on the linker length. Indeed, while $Ph_x$LPC assembled into closed ovoid structures, $Pyr_x$LPC led to the formation of rigid open sheets. In addition, $Pyr_x$LPC assemblies displayed a significant red shift and narrowing of the Q-band which was related to the formation of ordered J-aggregates. The experimental data were strongly supported by MD simulations highlighting the central role of the interaction between porphyrin cores rather than the length mismatch between the two phospholipids chains in controlling the structure of the lipid bilayer membranes and thus

their optical properties. Indeed, while $Ph_x$LPC have the tendency to form inter-leaflet π-stacked dimers, $Pyr_x$LPC conjugates formed dimers within the same leaflet. This explained the formation of hard open sheet observed for $Pyr_x$LPC and the undulated bilayers in the case of $Ph_x$LPC assemblies. In addition, the MD simulations shed light on the role of the linker in controlling the number of π-stacking events. For instance, the longer linker allowed the optimal π-stacking between the porphyrin moieties. Finally, both experimental and computational results demonstrated that these conjugates can be efficiently inserted in the lipid bilayer matrix with higher penetration depth for $Pyr_x$LPC compounds. Moreover, it appeared that the fluidity of the phospholipid bilayer is an important parameter to control whether J-aggregates of $Pyr_x$LPC can be formed or not. Altogether, this work could be used as guide for the design of new Pl-Por conjugates that self-assemble into supramolecular structures with tunable morphology and optical properties by playing with (i) the planarity and dipole moment of porphyrin core, (ii) the linker length and (iii) the structure of host lipid bilayer membrane.

## ASSOCIATED CONTENT

Electronic supplementary information (ESI) available.

## ACKNOWLEDGEMENTS

LGB is thankful to the French Ministry of Research for the financial support of his PhD thesis. The financial supports for Lipid-Porphyrin conjugates research from the ANR JCJC Grant (Project-ANR-19-CE09-0015) and from the Laboratory of Excellence LERMIT via an ANR grant (ANR-10-LABX-33) under the program of ‘‘Investissements d’avenir’’ are gratefully acknowledged. This project has received financial support from the CNRS through the MITI interdisciplinary programs. ÁT and F.D.M. were financially supported by the Agence Nationale

de la Recherche (ANR-19-CE17-0020-01 IMOTEP), Région Nouvelle Aquitaine and Institut National de la Santé et de la Recherche Médicale (AAP NA 2019 VICTOR). Authors are grateful to regional supercomputer facilities CALI ("CAlcul en LImousin") and Baba Yaga as well as to Xavier Montagutelli for technical support. This work was performed using HPC resources from GENCI–IDRIS (Grant 2021-A0100711487).

## References

1. J. N. Israelachvili, *Intermolecular and Surface Forces*, Academic Press, San Diego, 3rd edn., 2011.
2. J. N. Israelachvili, D. J. Mitchell and B. W. Ninham, *Biochimica Et Biophysica Acta*, 1977, **470**, 185-201.
3. V. V. Kumar, *Proc Natl Acad Sci U S A*, 1991, **88**, 444-448.
4. M. Ramanathan, L. K. Shrestha, T. Mori, Q. Ji, J. P. Hill and K. Ariga, *Physical Chemistry Chemical Physics*, 2013, **15**, 10580-10611.
5. X. Li, S. Lee and J. Yoon, *Chem Soc Rev*, 2018, **47**, 1174-1188.
6. I. Paramio, T. Torres and G. de la Torre, *ChemMedChem*, 2021, **16**, 2441-2451.
7. J.-Q. Cai, X.-M. Liu, Z.-J. Gao, L.-L. Li and H. Wang, *Materials Today*, 2021, **45**, 77-92.
8. M. Shakiba, K. K. Ng, E. Huynh, H. Chan, D. M. Charron, J. Chen, N. Muhanna, F. S. Foster, B. C. Wilson and G. Zheng, *Nanoscale*, 2016, **8**, 12618-12625.
9. J. F. Lovell, C. S. Jin, E. Huynh, H. Jin, C. Kim, J. L. Rubinstein, W. C. Chan, W. Cao, L. V. Wang and G. Zheng, *Nat Mater*, 2011, **10**, 324-332.
10. E. Huynh, B. Y. C. Leung, B. L. Helfield, M. Shakiba, J.-A. Gandier, C. S. Jin, E. R. Master, B. C. Wilson, D. E. Goertz and G. Zheng, *Nature Nanotechnology*, 2015, **10**, 325-332.
11. E. Huynh and G. Zheng, *Wiley Interdiscip Rev Nanomed Nanobiotechnol*, 2013, **5**, 250-265.
12. S. Matsubara and H. Tamiaki, *Journal of Photochemistry and Photobiology C: Photochemistry Reviews*, 2020, **45**, 100385.
13. J. Otsuki, *Journal of Materials Chemistry A*, 2018, **6**, 6710-6753.
14. M. A. Rajora, J. W. H. Lou and G. Zheng, *Chem Soc Rev*, 2017, **46**, 6433-6469.
15. E. Huynh and G. Zheng, *Nano Today*, 2014, **9**, 212-222.
16. T. D. MacDonald and G. Zheng, *Photonics & Lasers in Medicine*, 2014, **3**, 183-191.
17. C. S. Jin, J. F. Lovell, J. Chen and G. Zheng, *ACS Nano*, 2013, **7**, 2541-2550.
18. L. Cui, Q. Lin, C. S. Jin, W. Jiang, H. Huang, L. Ding, N. Muhanna, J. C. Irish, F. Wang, J. Chen and G. Zheng, *ACS Nano*, 2015, **9**, 4484-4495.
19. M. A. Rajora, L. Ding, M. Valic, W. Jiang, M. Overchuk, J. Chen and G. Zheng, *Chem Sci*, 2017, **8**, 5371-5384.
20. R. J. Paproski, A. Forbrich, E. Huynh, J. Chen, J. D. Lewis, G. Zheng and R. J. Zemp, *Small*, 2016, **12**, 371-380.
21. E. Chang, J. Bu, L. Ding, J. W. H. Lou, M. S. Valic, M. H. Y. Cheng, V. Rosilio, J. Chen and G. Zheng, *Journal of Nanobiotechnology*, 2021, **19**, 154.
22. K. A. Carter, S. Shao, M. I. Hoopes, D. Luo, B. Ahsan, V. M. Grigoryants, W. Song, H. Huang, G. Zhang, R. K. Pandey, J. Geng, B. A. Pfeifer, C. P. Scholes, J. Ortega, M. Karttunen and J. F. Lovell, *Nat Commun*, 2014, **5**, 3546.

23. D. M. Charron, G. Yousefalizadeh, H. H. Buzzá, M. A. Rajora, J. Chen, K. G. Stamplecoskie and G. Zheng, *Langmuir*, 2020, **36**, 5385-5393.
24. J. Massiot, V. Rosilio, N. Ibrahim, A. Yamamoto, V. Nicolas, O. Konovalov, M. Tanaka and A. Makky, *Chemistry – A European Journal*, 2018, **24**, 19179-19194.
25. A. D. Bangham, M. M. Standish and J. C. Watkins, *J Mol Biol*, 1965, **13**, 238-252.
26. M. M. da Cunha, S. Trepout, C. Messaoudi, T. D. Wu, R. Ortega, J. L. Guerquin-Kern and S. Marco, *Micron*, 2016, **84**, 23-36.
27. B. D. Madej, I. R. Gould and R. C. Walker, *The Journal of Physical Chemistry B*, 2015, **119**, 12424-12435.
28. C. J. Dickson, B. D. Madej, Å. A. Skjevik, R. M. Betz, K. Teigen, I. R. Gould and R. C. Walker, *Journal of Chemical Theory and Computation*, 2014, **10**, 865-879.
29. J. Wang, R. M. Wolf, J. W. Caldwell, P. A. Kollman and D. A. Case, *Journal of Computational Chemistry*, 2004, **25**, 1157-1174.
30. D. J. Price and C. L. Brooks, *The Journal of Chemical Physics*, 2004, **121**, 10096-10103.
31. L. Martínez, R. Andrade, E. G. Birgin and J. M. Martínez, *Journal of Computational Chemistry*, 2009, **30**, 2157-2164.
32. R. Salomon-Ferrer, D. A. Case and R. C. Walker, *Wiley Interdisciplinary Reviews: Computational Molecular Science*, 2013, **3**, 198-210.
33. D. R. Roe and T. E. Cheatham, *Journal of Chemical Theory and Computation*, 2013, **9**, 3084-3095.
34. H. Nguyen, D. R. Roe, J. Swails and D. A. Case, *Journal*, 2016.
35. D. P. Tieleman, S. J. Marrink and H. J. C. Berendsen, *Biochimica et Biophysica Acta (BBA) - Reviews on Biomembranes*, 1997, **1331**, 235-270.
36. C. J. Dickson, V. Hornak, R. A. Pearlstein and J. S. Duca, *Journal of the American Chemical Society*, 2017, **139**, 442-452.
37. R. Guixà-González, I. Rodriguez-Espigares, J. M. Ramírez-Anguita, P. Carrió-Gaspar, H. Martinez-Seara, T. Giorgino and J. Selent, *Bioinformatics*, 2014, **30**, 1478-1480.
38. W. Humphrey, A. Dalke and K. Schulten, *Journal of Molecular Graphics*, 1996, **14**, 33-38.
39. R. Rosseto and J. Hajdu, *Chem Phys Lipids*, 2010, **163**, 110-116.
40. R. Rosseto and J. Hajdu, *Chem Phys Lipids*, 2014, **183**, 110-116.
41. R. Rosseto and J. Hajdu, *Tetrahedron*, 2014, **70**, 3155-3165.
42. E. E. Jelley, *Nature*, 1936, **138**, 1009-1010.
43. F. Würthner, T. E. Kaiser and C. R. Saha-Möller, *Angewandte Chemie International Edition*, 2011, **50**, 3376-3410.
44. E. E. Jelley, *Nature*, 1937, **139**, 631-631.
45. G. Scheibe, L. Kandler and H. Ecker, *Naturwissenschaften*, 1937, **25**, 75-75.
46. J. Massiot, V. Rosilio and A. Makky, *Journal of Materials Chemistry B*, 2019, **7**, 1805-1823.
47. S. J. Marrink, V. Corradi, P. C. T. Souza, H. I. Ingólfsson, D. P. Tieleman and M. S. P. Sansom, *Chemical Reviews*, 2019, **119**, 6184-6226.
48. L.-G. Bronstein, P. Cressey, W. Abuillan, O. Konovalov, M. Jankowski, V. Rosilio and A. Makky, *J Colloid Interf Sci*, 2022, **611**, 441-450.
49. A. Wnętrzak, K. Łątka and P. Dynarowicz-Łątka, *The Journal of Membrane Biology*, 2013, **246**, 453-466.
50. J. F. Nagle, *Annual Review of Physical Chemistry*, 1980, **31**, 157-196.
51. D. Marsh, *Chemistry and Physics of Lipids*, 1991, **57**, 109-120.
52. K. A. Riske, R. P. Barroso, C. C. Vequi-Suplicy, R. Germano, V. B. Henriques and M. T. Lamy, *Biochimica et Biophysica Acta (BBA) - Biomembranes*, 2009, **1788**, 954-963.
53. L. M. Ickenstein, M. C. Sandström, L. D. Mayer and K. Edwards, *Biochimica et Biophysica Acta (BBA) - Biomembranes*, 2006, **1758**, 171-180.

54. M. J. Bowick and R. Sknepnek, *Soft Matter*, 2013, **9**, 8088-8095.
55. G. Vernizzi, R. Sknepnek and M. Olvera de la Cruz, *Proceedings of the National Academy of Sciences*, 2011, **108**, 4292-4296.
56. R. Sknepnek, G. Vernizzi and M. Olvera de la Cruz, *Soft Matter*, 2012, **8**, 636-644.
57. C.-Y. Leung, L. C. Palmer, B. F. Qiao, S. Kewalramani, R. Sknepnek, C. J. Newcomb, M. A. Greenfield, G. Vernizzi, S. I. Stupp, M. J. Bedzyk and M. Olvera de la Cruz, *ACS Nano*, 2012, **6**, 10901-10909.
58. J. F. Nagle and S. Tristram-Nagle, *Biochimica et Biophysica Acta (BBA) - Reviews on Biomembranes*, 2000, **1469**, 159-195.
59. Z. V. Leonenko, E. Finot, H. Ma, T. E. S. Dahms and D. T. Cramb, *Biophysical Journal*, 2004, **86**, 3783-3793.
60. C. Hoffmann, A. Centi, R. Menichetti and T. Bereau, *Scientific Data*, 2020, **7**, 51.
61. A. Ghysels, A. Krämer, R. M. Venable, W. E. Teague, E. Lyman, K. Gawrisch and R. W. Pastor, *Nature Communications*, 2019, **10**, 5616.
62. E. L. Elson, E. Fried, J. E. Dolbow and G. M. Genin, *Annual Review of Biophysics*, 2010, **39**, 207-226.